

Review

Self-Assembled Nanocomposites and Nanostructures for Environmental and Energy Applications

Sujie Chang ^{1,*} , Xiaomin Wang ¹, Qiaoling Hu ¹, Xigui Sun ¹, Aiguo Wang ¹, Xiaojun Dong ¹, Yu Zhang ², Lei Shi ¹ and Qilei Sun ^{1,*}

¹ School of Materials Science and Engineering, Shandong Jianzhu University, Fengming Road, Jinan 250101, China; wxm12345611@163.com (X.W.); h17865316580@163.com (Q.H.); sunxigui@sdjzu.edu.cn (X.S.); sdjzu2021wang@163.com (A.W.); dxj15610172605@163.com (X.D.); slcjq@sdjzu.edu.cn (L.S.)

² Shandong Institute of Mechanical Design and Research, Jinan 250031, China; zhangyuszt@qlu.edu.cn

* Correspondence: 13771@sdjzu.edu.cn (S.C.); sdaisun@sdjzu.edu.cn (Q.S.); Tel.: +86-1509-879-5090 (S.C.); +86-1336-105-5758 (Q.S.)

Abstract: Self-assembled nanocomposites are attracting considerable attention owing to their controllable architectures and self-assembly processes, as well as the increase in worldwide environmental effects and energy needs. Further understanding of the self-assembly procedure for improving environmental and energy applications would advance the design and manufacture of nanomaterials for various applications. These materials can be grouped into major categories for various application fields, including powder photocatalysts, membrane photocatalysts, and thin-film thermoelectric nanomaterials. These self-assembled nanomaterials can be used for environmental and energy applications, such as wastewater purification, hydrogen production by water splitting, energy storage, and energy harvesting. In this review, a brief introduction to the definitions and classifications of self-assembled nanocomposites is provided. We aim to provide a summary of the recent research related to self-assembled nanocomposites and nanostructures used for environmental and energy applications. Moreover, typical examples and discussions are aimed at demonstrating the advantages of self-assembled nanostructures. At the end of each section, the structural properties and the application of the nanocomposite or nanostructure are summarized. Finally, we provide perspectives for future research on the design and fabrication of self-assembled nanocomposites and nanostructures.

Keywords: nanocomposites; nanostructures; self-assembled; photocatalyst; energy materials; thermoelectric materials



Citation: Chang, S.; Wang, X.; Hu, Q.; Sun, X.; Wang, A.; Dong, X.; Zhang, Y.; Shi, L.; Sun, Q. Self-Assembled Nanocomposites and Nanostructures for Environmental and Energy Applications. *Crystals* **2022**, *12*, 274. <https://doi.org/10.3390/cryst12020274>

Academic Editor: Leonid Kustov

Received: 22 January 2022

Accepted: 14 February 2022

Published: 17 February 2022

Publisher's Note: MDPI stays neutral with regard to jurisdictional claims in published maps and institutional affiliations.



Copyright: © 2022 by the authors. Licensee MDPI, Basel, Switzerland. This article is an open access article distributed under the terms and conditions of the Creative Commons Attribution (CC BY) license (<https://creativecommons.org/licenses/by/4.0/>).

1. Introduction

It is well known that self-assembled nanocomposites and nanostructures are a class of molecules that spontaneously assemble directly through specific interactions or indirectly through their environment without any human intervention [1,2]. The benefits of self-assembled nanocomposites or nanostructures have been reported several times for their prominent applications. Thus, they are attracting widespread attention in environmental and energetic fields, as are their special self-assembled structures. The obtained nanocomposites and/or nanostructures have great potential in various applications [3–9].

There are a variety of reports about the methods and theories of self-assembly [10]. Furthermore, the types of self-assembled nanocomposites and nanostructures are diverse. In this review, self-assembled nanomaterials are classified as powder nanostructures, membrane photocatalysts, and thin-film thermoelectric nanomaterials.

Nanocomposites and nanostructures coupled to self-assembly processes can potentially exhibit significant advantages in environmental and energy applications [11–18]. With regards to self-assembled nanocomposites and nanostructures for environmental applications, we provide typical examples, such as wastewater purification using powder and

membrane nanomaterials and/or nanocomposites. Among them, TiO_2 has been recognized as one of the most promising materials for photocatalytic techniques due to its unique characteristics. The photocatalytic techniques using TiO_2 and TiO_2 -based materials have demonstrated appealing practical value, including wastewater purification and hydrogen evolution from water [19–23]. For energy applications, the self-assembly of nanocomposites and nanostructures has been used in conventional batteries, Li-ion batteries, energy storage, and energy harvesting. Self-assembled nanomaterials offer greatly improved ionic transport and electronic conductivities compared with those of conventional batteries and supercapacitor materials [24–26]. They can also occupy all available intercalation positions in the particle volume, resulting in high specific capacity and rapid ion diffusion. Due to these features, self-assembled nanomaterials are able to tolerate high currents, offering a prospective solution for high-power energy storage, including waste heat conversion. In this mini-review article, we mainly survey and discuss the classification of nanomaterials and nanocomposites, their general synthesis approaches, their primary characterization, and their special properties for environmental and energy applications. This review aims to highlight the significance of self-assembled nanostructures for their proposed applications. Finally, we conclude and present a future outlook for the further development of preferred materials for environmental and energy applications.

2. Self-Assembled Nanostructures Suitable for the Photocatalysis Process

2.1. Self-Assembled Nanostructured Powder Photocatalysts for Wastewater Treatment

With economic development and technological progress, water pollution has become a worldwide problem. Domestic sewage, agricultural sewage, and industrial wastewater have become significant sources of water pollution. Among them, industrial wastewater contains many forms of pollutants, creates large emissions, and is not easy to purify [19]. Traditional treatment methods mostly use physical deposition or chemical adsorption [20,27], are expensive, and have limited effectiveness. The photocatalytic degradation of organic pollutants as a new wastewater treatment technology has become a popular research topic in recent years [28,29], and metal oxide nanoparticles (titanium dioxide, zinc oxide, and iron oxide), carbon nanotubes, nanocomposites, and many other types of nanomaterials have been used as catalysts for wastewater treatment [30–33]. More specifically, some self-assembled nanophotocatalytic systems have been designed to degrade heavy metal ions, pharmacological waste, toxic organic molecules, volatile oxygen compounds (VOCs), etc., from waste water [34–42]. For example, Sun et al. prepared self-assembled BiOI/BiOCl microflowers by a coprecipitation method, which showed higher photocatalytic efficiency in photocatalytic oxidation of gas-phase mercury [37].

Liu et al. successfully prepared $\text{CdS}@\text{MoS}_2$ heterostructured nanocomposites with branching nanostructures by a hydrothermal method [29]. The advantages of the hydrothermal method are obvious [43]. They carried out degradation tests of methyl bromide under visible light and studied the photocatalytic activities of pure CdS , pure MoS_2 , and $\text{CdS}@\text{MoS}_2$ (5%) nanoparticles prepared with different Mo and Cd molar ratios through the photodegradation of methyl bromide (Figure 1a,b). The best photocatalytic performance was achieved by $\text{CdS}@\text{MoS}_2$ (5%) (Figure 1d,e), which exhibited a strong adsorption capacity (up to 36%) for methyl bromide with excellent long-term stability (Figure 1c).

Saif et al. prepared pure anatase titanium dioxide with a heterogeneous nanomorphology and micromorphology by controlling the hydrothermal reaction time [44]. The hydrothermal treatment of TiO_2 sols in aqueous acetic/nitric acid solutions enhanced the absorption of solar radiation, and they found that 24 h was the optimum preparation time for TiO_2 nanoparticles; the complexation of photogenerated electrons and holes could be most effectively suppressed when the TiO_2 photooxidation activity was at its highest.

In addition to this, metal-based hybrid nanostructures are being increasingly used as photocatalysts for wastewater treatment, and research into the combination of graphene and its derivatives with metal nanoparticles to form highly stable catalysts is receiving

increasing attention. Due to the large surface area of graphene, the dispersion of metal nanoparticles is effectively enhanced, thus improving the stability of the catalysts [45–47].

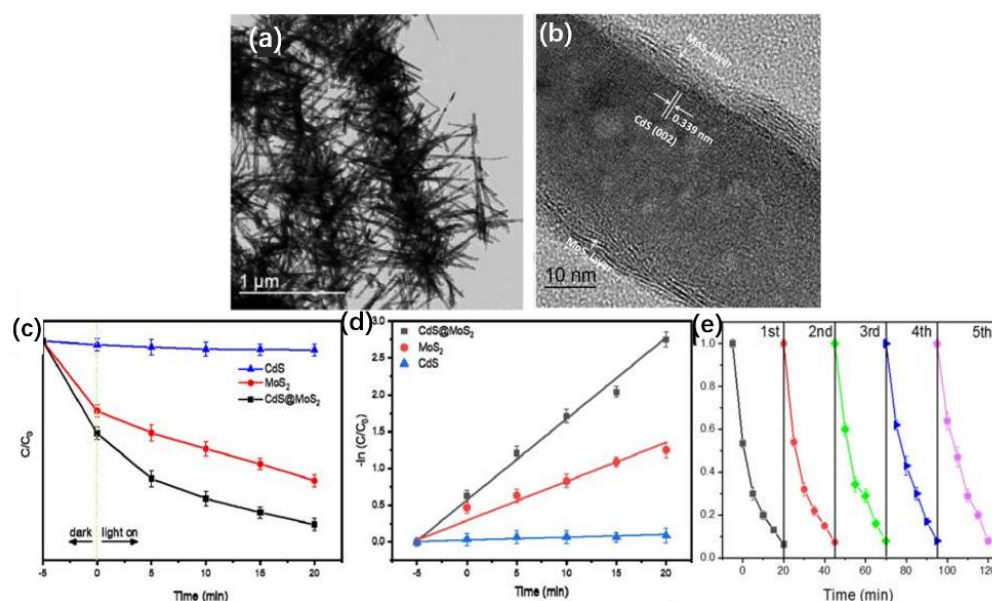


Figure 1. (a) Transmission electron microscopy (TEM) image of CdS@MoS₂ (5%). (b) High-resolution TEM (HRTEM) image of the obtained CdS@MoS₂ (5%) heterostructured nanocomposites (HSNPs). (c) Photocatalytic activities of pure CdS, pure MoS₂, and CdS@5%MoS₂ HSNP in the degradation of methyl blue (MB) by visible light irradiation and (d) corresponding linearized kinetics. (e) Different cycles of photocatalytic degradation of methyl bromide by CdS@5%MoS₂ HSNPs under visible light irradiation. Copyright © 2020 American Chemical Society.

Wang et al. prepared self-assembled phytic acid-graphene oxide composite foam (PAGF)@Au&Fe₃O₄ catalysts using a self-assembly technique with a hydrothermal method [48]. The larger surface area of graphene facilitated the loading of gold nanoparticles and improved their dispersion, and the stability of the catalysts was greatly enhanced by the addition of Fe₃O₄. A new porous ACS-ZnO nanocomposite was prepared by a self-assembly technique with a hydrothermal reaction by loading ZnO nanoparticles onto the porous skeleton of *Halocystis* sp. [49]. The nanocomposites with different ZnO contents were put into three dyes, methyl blue (MB), rhodamine B (RhB), and neutral red (NR). The photodegradation effects of the Artemia cyst shell -ZnO (ACS-ZnO) nanocomposites were significantly stronger than those of the pure ZnO nanoparticles, and the composite with 40% ZnO content had the strongest catalytic ability for the three dyes. An eight-cycle experiment showed the high stability and sustainable use of this composite.

Liu et al. prepared a polyvinyl alcohol (PVA)/polyacrylic acid (PAA)/silver-nanoparticle-modified carboxy-functionalized graphene oxide (PVA/PAA/GO-COOH@AgNPs) by electrostatic spinning and heat treatment techniques [50]. In this novel multifunctional catalyst, the nanofiber structure effectively prevented the agglomeration of silver nanoparticles and improved the stability of the photocatalysis. The strong π - π forces in the graphene oxide (GO) sheets and the highly negatively charged carboxyl groups immobilized within the GO nanosheets promoted the diffusion of the target dye and enhanced the catalytic degradation of MB through strong adsorption and strong electrostatic interactions, and the catalytic amount of MB was maintained at ca. 26.32 mg/g after eight consecutive cycles for the PVA/PAA/GO-COOH@AgNPs nanocomposite film (ca. 99.8% compared to 26.36 mg/g in the first catalytic process), demonstrating its remarkable catalytic activity, undergoing eight catalytic degradation cycles at room temperature, thus indicating its promising application in wastewater treatment.

The main disadvantages of using nanomaterials in wastewater treatment are the separation step and the high operational costs. To improve the recycling of nanocatalysts,

researchers have proposed magnetic nanoparticles or nanocomposites [51]. Magnetic nanomaterials are easy to separate, highly recyclable, and do not lose their photocatalytic activity in different applications.

Yang et al. successfully prepared an Fe₃O₄ magnetic fluid and an amorphous Fe-B magnetic fluid by chemical reduction and applied them to the deep treatment of high-concentration organic wastewater [52]. The removal rate of the amorphous Fe-B magnetic fluid for organic matter in the wastewater was up to 96%, and the decolorization effect was increased by 20% compared to that of the Fe₃O₄ magnetic fluid, mainly due to the high activity of amorphous Fe-B nanoparticles. The catalytic activity was enhanced by its surface and special amorphous structure; this increases the efficiency of wastewater treatment.

2.2. Self-Assembled Nanostructured Powder Photocatalysts for Photocatalytic Hydrogen Production

The development of pollution-free technologies for environmental management and alternative clean energy supplies is an urgent task for the sustainable development of society.

In 1972, Fujishima and Honda first discovered the photodegradation of water to produce hydrogen at a TiO₂ electrode. This opened up the possibility of using solar energy to decompose water to produce hydrogen, and since then, researchers have been working on the development of various oxide photocatalysts [19]. Of these, transition metal oxide semiconductors (TiO₂ and ZnO) have been widely used as photocatalysts due to their safety, low costs, narrow bandgaps, and environmental stability, but their low absorption in visible light has hindered their application in photocatalysis [14]. Enhancing their visible light absorption and photocatalytic efficiency has become an important research direction.

Peng et al. investigated the capture of CdS nanoparticles in TiO₂ nanotubes treated at different temperatures and showed that the CdS nanoparticles captured in the TiO₂ nanotubes had better hydrogen production activity than CdS nanoparticles loaded on the outside of the TiO₂ nanotubes [27]. The CdS nanoparticles captured in the TiO₂ nanotubes had good TiO₂ crystallinity, and they are a promising photocatalyst for visible-light hydrogen production.

Yendrapati et al. proposed a method for efficient hydrogen precipitation using tunable ZnO nanorods modified with Cu composites and prepared ZnO@CuS heterogeneous nanostructures using a simple hydrothermal reaction (Figure 2a,b) that still exhibited significantly enhanced photocatalytic hydrogen precipitation activity without the use of any noble metal cocatalysts [28]. While characterizing their optical and photophysical properties, the pristine ZnO nanorods were compared, and it was found that zinc oxide nanorods (ZCS2) with the addition of 2% CuS nanoparticles could enhance absorption in the visible region (Figure 2c) and could significantly increase the photocatalytic hydrogen production (10,113.59 μmol/g·h) (Figure 2d), which was nearly 35 times that of the pristine ZnO photocatalyst. The results indicated that in terms of the charge migration mechanism, the construction of heterojunctions can achieve a visible light response, efficient separation of electron holes, and improved photocatalytic hydrogen production activity. The excellent photocatalytic activity of the material was mainly due to the improved light capture capability, the effective charge separation during photocatalysis, and the synergistic effect of CuS and ZnO in the nanostructure assembly. The transport of the photoexcited charge through the heterojunction between ZnO and CuS facilitated the rapid movement of the photoexcited charge [29,53], which resulted in the enhancement of catalytic hydrogen production activity.

Wu et al. synthesized cross-linked microporous three-dimensional (3D) reduced graphene (rGO) hydrogels embedded with copper nanoparticles using graphite and copper acetate as raw materials by in situ photoreduction [54]. An 11.3% content of copper nanoparticles contributed to photocatalytic activity and achieved an optimum hydrogen precipitation rate of 16.92 mmol/g·h, indicating the potential use of copper nanoparticles in photocatalytic hydrogen production processes.

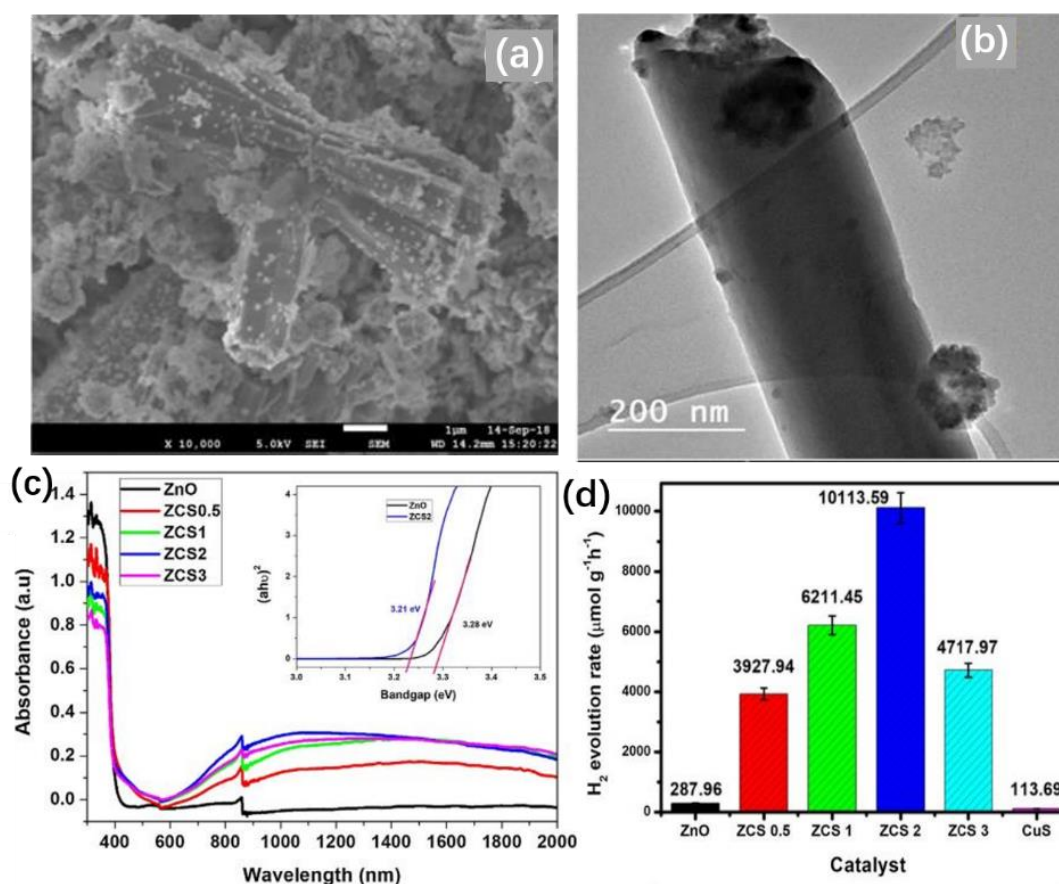


Figure 2. (a) Field emission scanning electron microscopy (FESEM) image of ZnO@CuS (2%) nanocomposite. (b) TEM image of ZnO@CuS (2%) nanorods. (c) Ultraviolet (UV)–visible (vis) diffuse reflectance spectra of pristine ZnO and ZnO/CuS nanocomposite. The inset shows the Tauc plots for ZnO and ZCS2. (d) Comparison of photocatalytic H₂ production rates of all the samples. Copyright © 2021 Elsevier B.V.

Metal nanoparticles have weak interactions and a single form, and thus, they are difficult to orientate and self-assemble. Compared to monometallic nanoparticles, bimetallic nanoparticles show good catalytic properties due to the synergy between the two metals [54,55].

Ding et al. obtained metal nanoparticles that were deposited at the edges of the CaIn₂S₄ nanosteps, indicating that photogenerated electrons were more readily available for reduction reactions at the edges of the nanosteps [51]. The ultraviolet (UV)–visible (vis) absorption spectra (Figure 3c) showed that the different bimetallic nanostructures exhibited different absorption properties. Pure CaIn₂S₄ had an absorption range from approximately the UV region to around 450 nm. Au_{0.5}/CaIn₂S₄ had a larger absorption range, mainly due to the metal surface plasmon resonance effect of the gold nanoparticles. Cu_{0.5}/CaIn₂S₄ was weaker in the visible range, which was caused by the scattering effect of the Cu nanoparticles. For the alloyed A4C1/CIS composites, the addition of Cu forms an AuCu alloy structure where the visible absorption weakens and the Au blue-shifted SPR peak reaches shorter wavelengths due to the reduced size and content of the Au nanoparticles, and for the core–shell C1/A4/CIS composites, the Au nuclei are covered by the Cu shell layer, the Au SPR band disappears, and the optical contribution of the Au nuclei is substantially reduced. The Au–Cu alloy structure was more favorable for the effective absorption of visible light than the AuCu core–shell structure, and the alloy structure of AuCu bimetallic nanoparticles (452.8 μmol/h) was more favorable for photocatalytic hydrogen production than the core–shell structure (205.7 μmol/h).

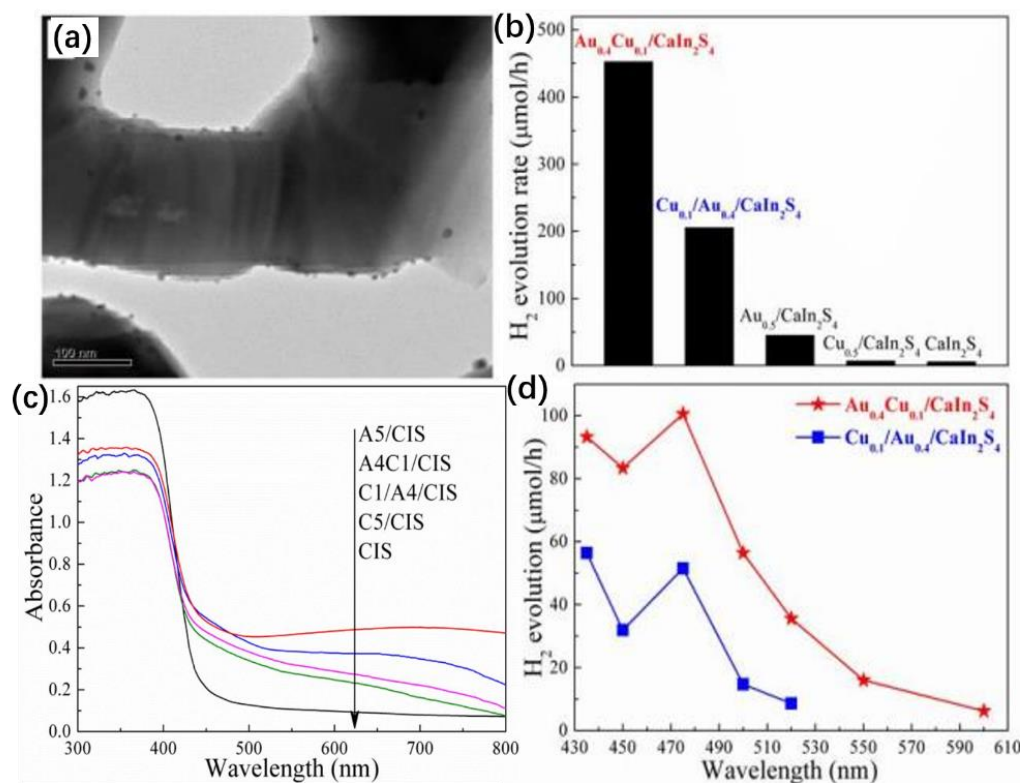


Figure 3. (a) TEM image of Au_{0.4}Cu_{0.1}/CaIn₂S₄ composite. (b) Hydrogen production rate of Au_{0.5-x}Cu_x/CaIn₂S₄ (A_{0.5-x}C_x/CIS) composites with different contents of Cu. (c) UV-vis absorption spectra of Au_{0.5}/CaIn₂S₄ (A5/CIS), Au_{0.4}Cu_{0.1}/CaIn₂S₄ (A4C1/CIS), Cu_{0.1}/Au_{0.4}/CaIn₂S₄ (C1/A4/CIS), Cu_{0.5}/CaIn₂S₄ (C5/CIS), and CaIn₂S₄ (CIS). (d) Photocatalytic hydrogen production rate over Au_{0.4}Cu_{0.1}/CaIn₂S₄ and Au_{0.4}Cu_{0.1}/CaIn₂S₄ composites as functions of the incident light wavelength. Copyright © 2018 Elsevier B.V.

3. Self-Assembled Nanostructured Membranes for Photocatalysis

3.1. Self-Assembled Nanostructured Membrane Photocatalysts for Wastewater Treatment

Over the past few decades, membrane technology has proven to be a reliable and excellent alternative to traditional treatment technologies for clean water purification and wastewater treatment [56]. Nanomembrane materials are highly reusable, with membrane technology able to break down contaminants and leave little residue [57]. In particular, semiconductors like titanium dioxide (TiO₂) are of great interest due to their ability to mineralize all organic compounds under UV irradiation.

Liu et al. prepared titanium dioxide films via a layer-by-layer self-assembly technique to immobilize TiO₂ nanoparticles using polyurethane (PU) and increase the adsorption capacity of the photocatalyst [58]. In addition, the photocatalytic performance and reusability of the films were investigated by the decomposition of MB under UV irradiation, and it was shown that the catalytic efficiency of the prepared films was still as high as 94.56% after five cycles and they could be reused six times without affecting the photocatalytic activity. Synthetic membranes are therefore promising candidate materials for wastewater treatment applications.

However, single nano-TiO₂ photocatalysts have low specific surface area, poor adsorption capacity for pollutants, and are easily agglomerated and difficult to recover, resulting in low catalytic efficiency for the photocatalytic degradation of low concentrations of organic matter. The researchers found that composite nano-TiO₂ materials can significantly improve the defects of single nano-TiO₂ materials which are prone to agglomeration. To overcome the defects of nano-TiO₂ particles, research and application of composite materials are gaining increasing attention [21–23].

Zhang et al. successfully coated TiO₂ nanofibers onto ceramic hollow fiber membranes using a simple dip-coating technique to form TiO₂ nanofiber membranes with reticular morphologies (Figure 4a), and they evaluated the performances of the TiO₂ nanofiber membranes in treating hyaluronic acid by monitoring the change in the total organic carbon values in water [59]. After six cycles, there was no significant loss of activity of the TiO₂ nanofiber hollow membrane (Figure 4c). Therefore, the TiO₂ nanofiber hollow membranes proposed possessed high stability during the removal of hyaluronic acid.

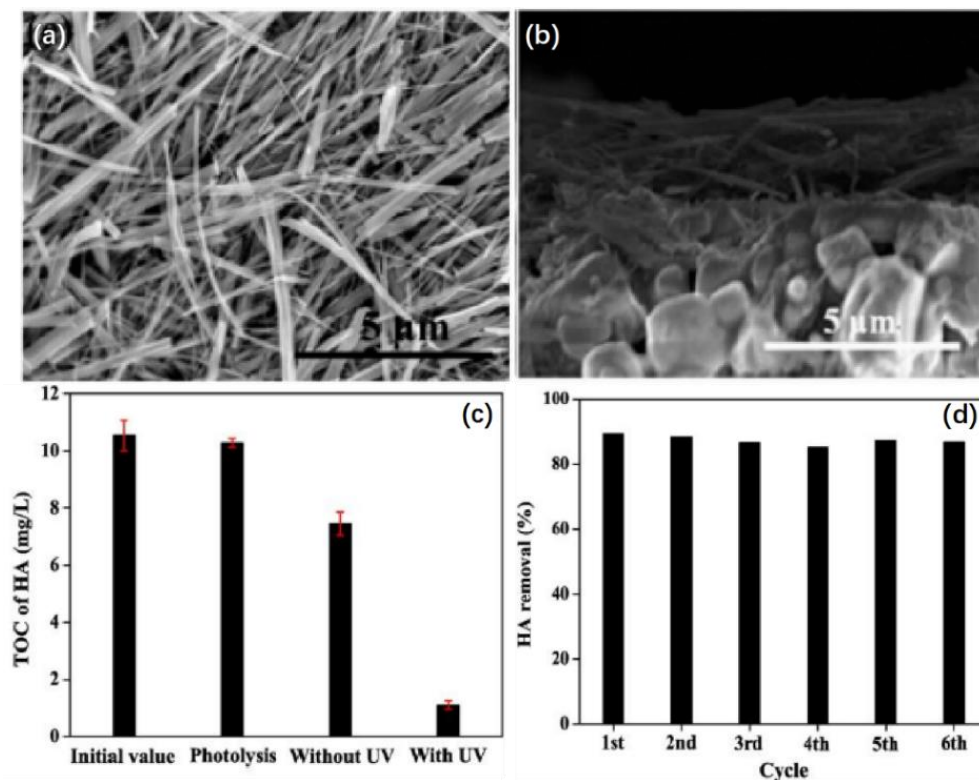


Figure 4. (a) Scanning electron microscopy (SEM) image of TiO₂ nanofibers synthesized by the hydrothermal method. (b) SEM image of ceramic hollow membranes coated with TiO₂ nanofibers. (c) Total organic carbon (TOC) removal using TiO₂ nanofiber membranes. (d) Reusability of the TiO₂ nanofiber membranes for hyaluronic acid removal. Copyright © 2015 Elsevier B.V.

Bai et al. successfully synthesized a novel multifunctional carbon nanotube/ZnO/TiO₂ nanocomposite ultrafiltration membrane by hydrothermal synthesis and ultrasonic-assisted acid treatment [60]. Chang et al. obtained self-assembled nanoporous Ti with a smooth surface and many folds by a hydrothermal method using metallic titanium foam as the raw material (Figure 5a,b) [61]. A self-assembled layer of a strongly adherent 3D Na₂Ti₃O₇ nanowire network was grown on the surfaces of Ti particles and channels after alkaline hydrothermal treatment in a NaOH solution (Figure 5c). The self-assembled TiO₂ nanowire networks were uniform, with lengths of 2–3 μm (Figure 5d) [61]. The self-assembled nanowire network utilized the wastewater degradation device shown in Figure 5e for two different types of dyes, RhB (20 mg/L, Figure 5f) and MB (20 mg/L, Figure 5g), both of which showed good photocatalytic properties after UV irradiation for 60 min only, reflecting its good degradation effects. The above results illustrate the high performance of self-assembled nanoporous Ti as photoelectrolytic electrode materials.

In addition, Fe₃O₄-based nanocomposites can be used as good Fenton-like catalysts for the degradation of organic pollutants in water [62]. The introduction of magnetic Fe₃O₄ nanoparticles provides another advantage for nanostructured composites, and the magnetic properties of the prepared composites facilitate fast and easy separation during catalyst recovery and reuse [63].

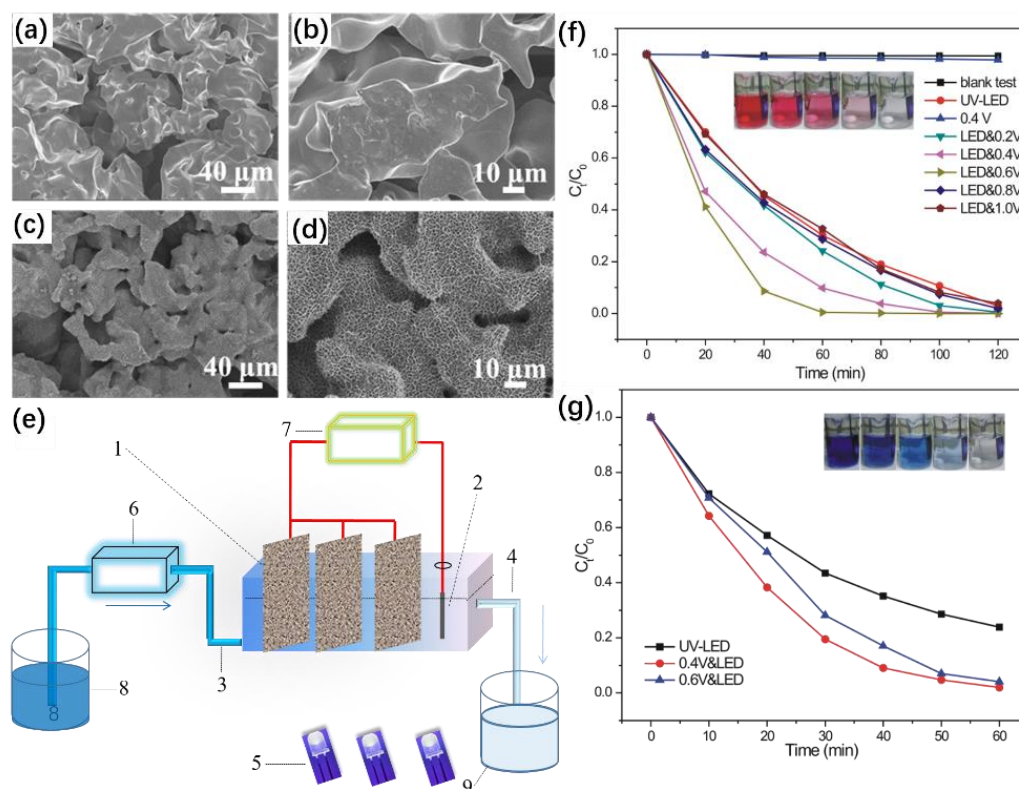


Figure 5. (a,b) SEM images of porous Ti. (c) Na₂Ti₃O₇/porous Ti. (d) SEM images of the cross-section of TiO₂/porous Ti with different magnifications. (e) Schematic diagram of the experimental reactor system: 1—TiO₂/porous Ti, 2—Pt wire electrode, 3—water inlet, 4—water outlet, 5—UV-light-emitting diodes (LEDs), 6—peristaltic pump, 7—electrochemical workstation, 8—sewage pool, and 9—recovered water pool. (f) C_t/C_0 vs. t and (g) MB degradation (20 mg/L) using TiO₂/porous Ti under photoelectrocatalysis (PEC) conditions. Copyright © 2017 Elsevier B.V.

Wang et al. successfully prepared an Fe₃O₄/rGO/metal–organic framework (MOF) composite with a dispersed interlayer structure by a hydrothermal method (Figure 6a) and investigated the degradation performances of these composites on phenol [64]. They found that the degradation of phenol was mainly dependent on the pH, and the degradation efficiency of phenol reached 80% within 2 min at pH = 3. The degradation rate of phenol decreased sharply when the pH was further reduced [65]. The phenol was completely removed within 16 min for all pH conditions (Figure 6b). By exploring the role of the catalyst components in Fenton-like reactions (Figure 6c), they found that the excellent catalytic performances of the Fe₃O₄/rGO/MOF composites were mainly due to the synergistic effect of the porous MOF shell and the internal Fe₃O₄/rGO [66]. The reusability of Fe₃O₄/rGO/MOF was tested by recovering the catalyst at the end of the reaction and reusing it in the next run. As shown, the catalytic activity of Fe₃O₄/rGO/MOF was maintained at 96% after five reuses (Figure 6d).

3.2. Self-Assembled Nanostructured Membrane Photocatalysts for Photocatalytic Hydrogen Production

The use of solar energy for photocatalytic hydrolysis to produce clean energy is currently an important means to address the depletion of fossil fuels. Achieving high photocatalytic efficiency, effective charge separation, and increased photocatalytic activity is currently a major problem. The common methods currently used are the construction of heterojunctions [67], the introduction of impurity atoms to regulate the electronic structure [68], and changing the crystalline surface or shape of the photocatalyst to facilitate space photocatalytic charge separation [69].

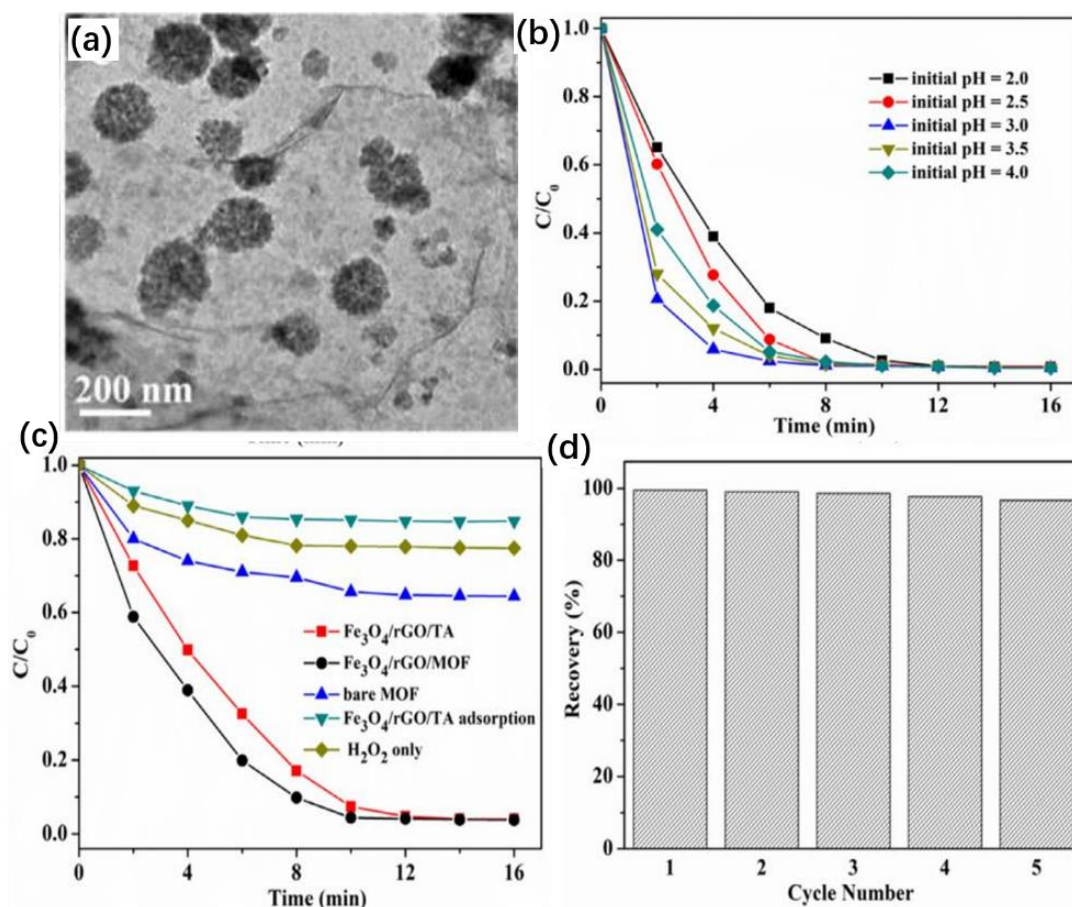


Figure 6. (a) TEM image of the as-prepared Fe_3O_4 /reduced graphene oxide (rGO)/metal–organic framework (MOF). (b) Effect of initial pH on degradation of phenol. (c) Effect of catalyst dose on the degradation of phenol. (d) Reusability of Fe_3O_4 /rGO/MOF. Copyright © 2019 Taiwan Institute of Chemical Engineers.

Photocatalyst modification using doped noble metal nanoparticles is an effective method to improve the photocatalytic performance. Dal’Acqua et al. prepared a multilayer composite by combining gold (Au) and titanium dioxide (TiO_2) nanoparticles (NPs) into self-assembled photocatalytic films (SAPFs) (Figure 7a) [70], forming a composite with larger specific surface area compared to those of conventional nanostructured catalysts. This facilitated the maximization of the photocatalytic activity. In this structured photocatalyst, hydrogen is produced in the polymer/(TiO_2 -Au) nanoparticle network and also in the body of the polymer/(TiO_2 -Au) NP assembly. Hydrogen is readily produced in large quantities under radiation, and the amount of hydrogen produced by the structured photocatalyst increased linearly with increasing UV irradiation time (Figure 7b). The SAPFs have great potential for renewable energy development due to their simple preparation process and excellent photocatalytic activity.

He et al. prepared nanoporous CoFe_2O_4 loaded with platinum and silver by dealloying [71]. They showed that the hydrogen precipitation rate of the resulting sample was as high as 2.36 mmol/h/g under full-spectrum irradiation, which was 24 times that of CoFe_2O_4 without platinum or silver (Figure 7c). The H_2 -releasing activity did not decrease significantly after 32 h of continuous irradiation (Figure 7d), indicating the excellent stability of this photocatalyst. The analysis showed that the silver NPs had a strong surface plasmon resonance (SPR) effect in visible light, resulting in effective visible light absorption. This effect expanded the range of light absorption and effectively improved light utilization, while Pt could act as an effective electron trap for electron–hole pair separation, effectively inhibiting electron and hole complexation. In addition, the simultaneous

loading of Pt and Ag on CoFe_2O_4 produced a synergistic effect that contributed to its photocatalytic performance.

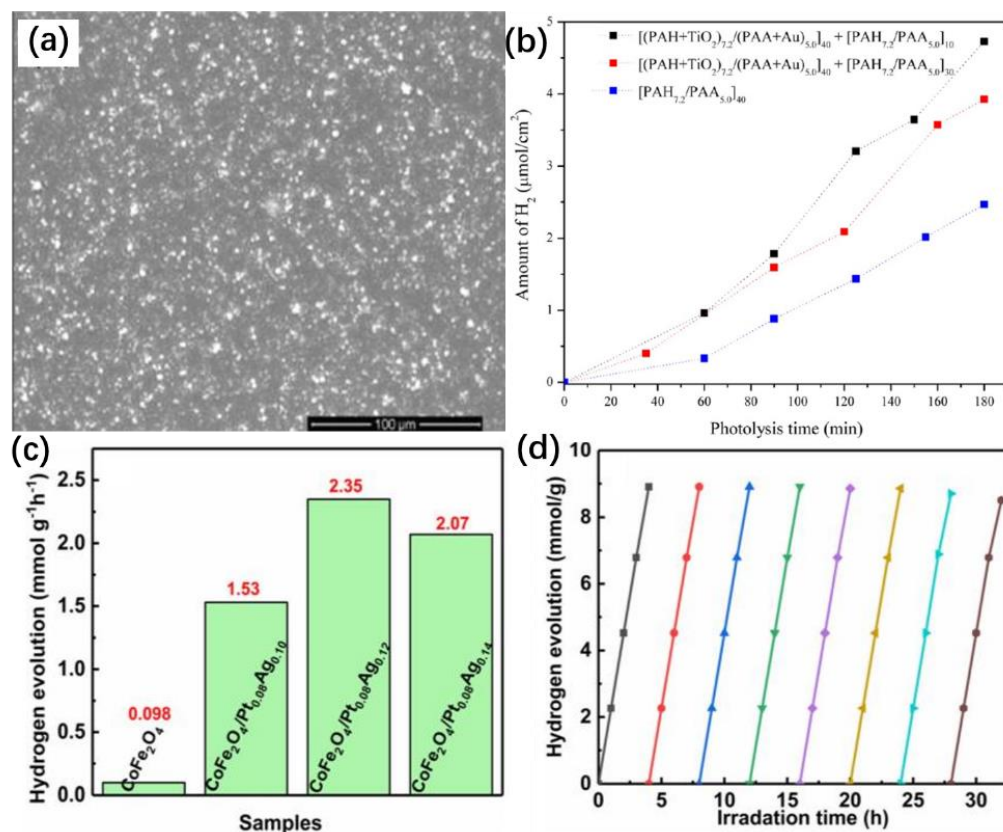


Figure 7. (a) SEM images of self-assembled photocatalytic films (SAPF) with 60 layers on a silicon substrate. (b) Hydrogen evolution in aqueous solution of methanol when films were irradiated with a 300-W Xe/Hg lamp. Copyright © 2013 American Chemical Society. (c) Average photocatalytic hydrogen evolution rates of CoFe_2O_4 , $\text{CoFe}_2\text{O}_4/\text{Pt}_{0.08}\text{Ag}_{0.10}$, $\text{CoFe}_2\text{O}_4/\text{Pt}_{0.08}\text{Ag}_{0.12}$, and $\text{CoFe}_2\text{O}_4/\text{Pt}_{0.08}\text{Ag}_{0.14}$ under full-wave irradiation. (d) Cycling measurements of photocatalytic hydrogen production of $\text{Pt}_{0.08}\text{Ag}_{0.12}/\text{CoFe}_2\text{O}_4$. Copyright © 2021 Springer Nature Switzerland AG.

The morphological modification of photocatalysts and the construction of heterojunctions are considered to be the main means of significantly improving the performances of photocatalytic hydrogen evolution [72,73].

Zhang et al. successfully synthesized ZnS nanocrystals with different morphologies using cysteine as the sulfur source at different heating temperatures using a template-free method (Figure 8a,d) and evaluated the photocatalytic performances of the samples [74]. After a series of catalytic experiments, it was found that the inherent self-absorption and photon recirculation of photoluminescence played a key role in the photocatalysis (Figure 8e). The photocatalytic activity was investigated by the degradation of RhB solutions. It is well known that the morphology of a material has an important influence on its properties. As shown by the photocatalytic results (Figure 8f) and the morphological images, ZnS-200 exhibits a simpler surface structure and better catalytic activity than ZnS-100 and ZnS-150, suggesting the idea that defect-rich edge states are advantageous in providing reactive sites and broadening the absorption range.

Bhirud et al. prepared hierarchical nanostructures of cubic-spinel-structured CdIn_2S_4 selectively by a hydrothermal method [75]. The effects of surfactants on the morphology and microstructure of cadmium sulfide were investigated using polyvinylpyrrolidone (PVP) and cetyltrimethylammonium bromide as surfactants. The cadmium sulfide samples prepared with PVP as the surfactant exhibited excellent photocatalytic activities, with a maximum hydrogen production rate of up to 3238 $\mu\text{mol}/\text{h}$.

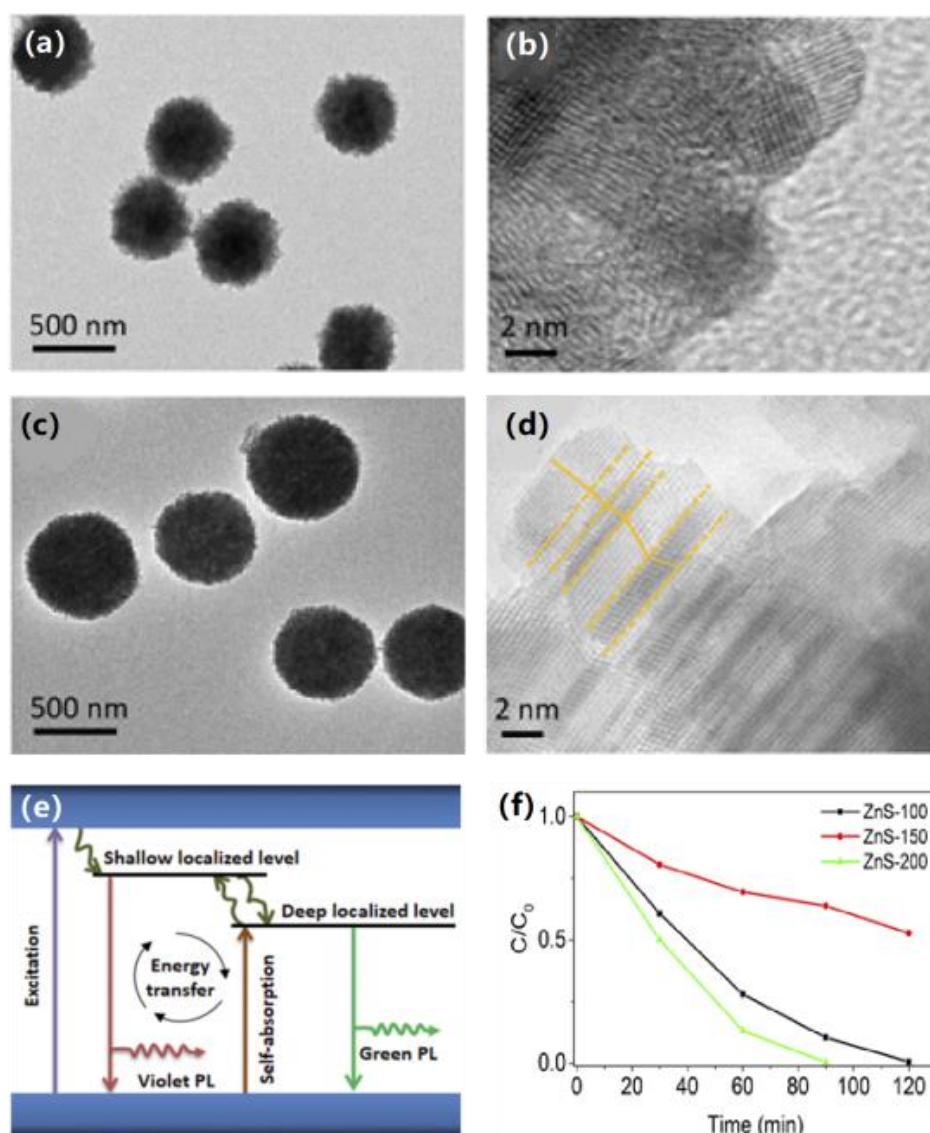


Figure 8. (a) TEM and (b) HRTEM images of ZnS-100. (c) TEM and (d) HRTEM images of ZnS-150. (e) Schematic illustration of electron transfer and proposed mechanism for photocatalytic performance. (f) Photocatalytic performances of samples for degradation of MB under xenon lamp irradiation. Copyright © 2020 Clarivate.

4. Self-Assembled Nanocomposites for Energy Storage

4.1. Self-Assembled Nanocomposites for Lithium-Ion Batteries

Lithium-ion batteries are widely used in various energy storage applications due to their good cycling performances and high energy densities. Traditional lithium-ion batteries mainly use graphite as the anode material, the surfaces of which are prone to the formation of lithium dendrites. Dendrite formation leads to a reduction of cycling stability and affects the service life of the battery. Thus, the development of electrode materials with high energies, high functional densities, and good cycling performances has become a popular research subject [76,77]. The electrode materials of new lithium batteries are often transition metals [78] which have large storage capacities, but their severe volume expansion during charging and discharging and poor electrical conductivities limit their practical application [79,80]. The high surface-to-volume ratio and high surface free energy of nanostructures are the keys to solving these issues [81,82]. Nanostructures can provide a shorter path for the transport of electrons and lithium ions, resulting in good conductivity and fast charge/discharge rates.

Deng et al. reported a simple wet chemistry route for the large-scale synthesis of nearly monodispersed self-assembled SnO₂ nanospheres by direct hydrogen peroxide oxidation of bulk tin (Sn) metal in deionized water (DIW) with the assistance of polyvinylpyrrolidone (PVP) and ethylenediamine (EDA) at room temperature, using PVP as a spatial stabilizer to limit the nanocrystal-to-nanocrystal contact, effectively preventing aggregation of nanocrystals [83] and causing particle aggregation to form nanospheres by minimizing the energy. The amount of PVP in the reaction system could lead to the controlled growth and self-assembly of SnO₂ nanocrystals. This study contributed to the large-scale synthesis of self-assembled functional oxide nanostructures. Man et al. prepared SnO₂ porous nanotubes (PNTs) by electrostatic spinning self-assembly (Figure 9a) [84]. The hollow structure and nano-SnO₂ particles effectively increased the contact area between the electrolyte and the active material, alleviated the defects caused by volume expansion, and improved their electrochemical properties. It was found through testing that the SnO₂-PNTs had excellent rate performances (Figure 9b). After charge/discharge tests, the coulombic efficiency exceeded 99% and could still provide a reversible capacity of 1045 mAh/g after 160 cycles (Figure 9c). As shown in the SEM images, there were no cracks on the electrode surface after cycling (Figure 9d), indicating its excellent structural stability.

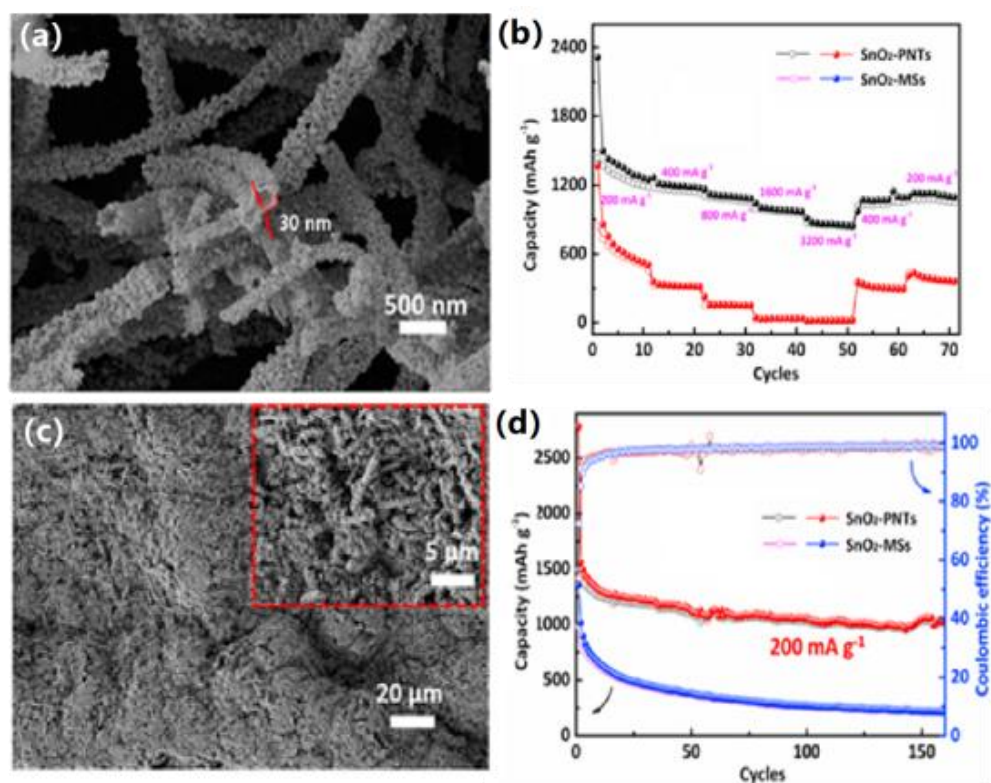


Figure 9. (a) SEM image of SnO₂ porous nanotubes (SnO₂-PNTs). (b) Rate performances of SnO₂-PNTs and commercial SnO₂ microspheres (SnO₂-MSs). (c) SEM image of SnO₂-PNTs after 100 cycles; the inset shows the partially enlarged view. (d) Cycling performances of SnO₂-PNTs and SnO₂-MSs at a current density of 200 mA/g. Copyright © 2008 American Chemical Society.

Molybdenum disulfide (MoS₂) is a layered transition metal disulfide that has also attracted interest as an electrode material for lithium batteries due to its important mechanical, electrical, and optical properties. It has been found that the addition of carbon-based conductive additives to MoS₂ can significantly improve the recyclability and testability of a material [85,86]. Das et al. prepared MoS₂-carbon hierarchical nanostructures with different carbon compositions by hydrothermal self-assembly and investigated the application of the composite as a high-energy electrode for lithium-ion secondary batteries [87]. When the material was used as an electrode for lithium batteries, the binding of carbon provided sig-

nificantly improved cycling stability and the carbon skeleton effectively inhibited particle agglomeration. Figure 10a shows that the MoS₂-carbon nanocomposite exhibited excellent stability, with the MoS₂-carbon nanocomposite containing 22% carbon (MS-22) showing the best stability.

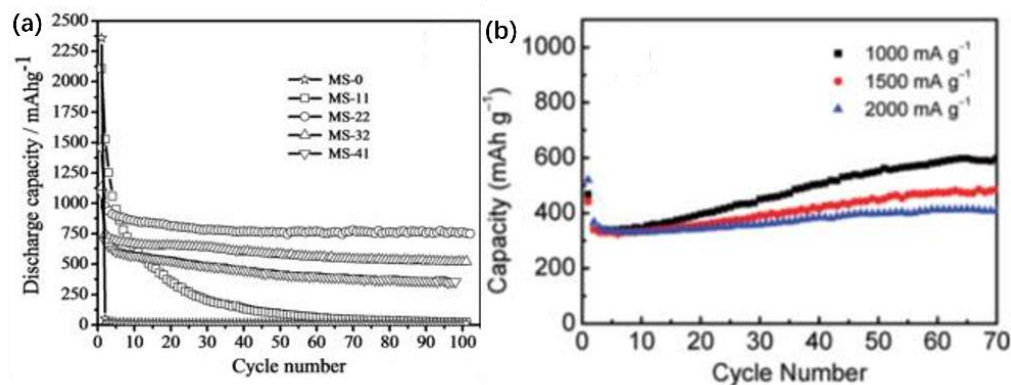


Figure 10. (a) Cycling stability of pure MoS₂ and various MoS₂-carbon composites. (b) Cycling performance of the MoO₂/graphene composite electrodes in the range of 3–0.01 V vs. Li at current densities of 1000, 1500, and 2000 mA/g. Copyright © 2011 American Chemical Society.

Carbon coatings usually cover the surface of an active material tightly and do not effectively release the large strain from the volume expansion, which in turn leads to increased resistance for the lithium ions to reach the active material inside. Graphene is used as a nanostructured electrode material for energy applications due to its special structure, excellent electrical conductivity, large surface area, and chemical stability [88].

Sun et al. realized the large-scale preparation of MoO₂/graphene nanocomposites by uniformly encapsulating MoO₂ nanocrystals in graphene sheets and testing them as the positive electrodes of lithium-ion batteries. They found that the electrode material synthesized from MoO₂/graphene nanocomposites had a significantly higher electrochemical performance than the bare MoO₂ electrode material [89]. The electrochemical performance of the MoO₂/graphene nanocomposite was found to be significantly higher than that of the bare MoO₂ electrode material, with high cyclability and increasing reversible capacity. The coulomb efficiency approached 100% at high current densities, and the capacity reached up to 407.7 mAh/g after 70 cycles and up to 848.6 mAh/g at low current densities (Figure 10b). The morphology remained pristine, further demonstrating the high stability of the graded nanostructures, excellent cycling performances, and good rate capability.

MOFs or porous coordination polymers have received special attention as a new class of hybrid nanoporous materials because of their high surface areas and unique structure [90,91]. Zhu et al. prepared porous ZnO/Co₃O₄ nanocomposite clusters by self-assembly [92], with an initial discharge capacity of up to 2049 mAh/g, which showed high reversible capacity of 957 mAh/g after 100 cycles.

4.2. Self-Assembled Nanostructured Supercapacitor Materials

The excessive use of fossil fuels, such as coal, oil, and natural gas, has led to a combination of energy growth and environmental problems, which has attracted attention [93]. Therefore, it is necessary to improve power generation efficiency and develop clean and efficient energy conversion and storage methods, and supercapacitors have the potential to meet the huge energy demand and advanced technical requirements [94–96]. The importance of supercapacitors has become increasingly prominent, and considerable in-depth research on their manufacturing technology and applied materials has been performed. Metal oxide supercapacitor electrodes are expensive and have low conductivities and poor stabilities, which limit their practical application. The research on self-assembled nanomaterials provides solutions to these problems. This section introduces the nanostructures based on self-assembly technology applied to supercapacitors, such as nanothickness MnO₂ nanosheets, carbon nanotubes, graphene, silicon carbide nanowires, activated carbon

films, Sm_2O_3 nanoparticles (SMNs), and deoxyribonucleic acid (DNA)-like double helix WO_{3-x}/C superstructures.

A composite of polycation-functionalized reduction of graphene oxide (FRGO-p) and MnO_2 nanosheets (FRGO-p- MnO_2) was synthesized by the electrostatic precipitation method [97] (Figure 11). Since the self-assembly of the MnO_2 sheet effectively prevented the aggregation of MnO_2 , this material showed a strong capacitive performance and retained more than 89% of its initial capacitance after 1000 cycles. The layered nanostructure was prepared by an electrostatic self-assembly method [98]. The capacitance of the graphene supercapacitor was increased by more than 70%, the high-power density was increased by 15%, and the cycle life was increased. A graphene/carbon nanotube hybrid film with an interconnected carbon structure network was prepared by layer-by-layer (LBL) self-assembly technology [99]. The pure carbon electrode based on amine-based functionalized multi-walled carbon nanotubes (MWCNT- NH_2) and rGO self-assembly prepared by Byon et al. had a specific capacitance of 120 F/g. The specific capacitance of the MWCNT/rGO electrode assembled by hydrazine steam treatment was about 1.5 times higher than that of rGO.

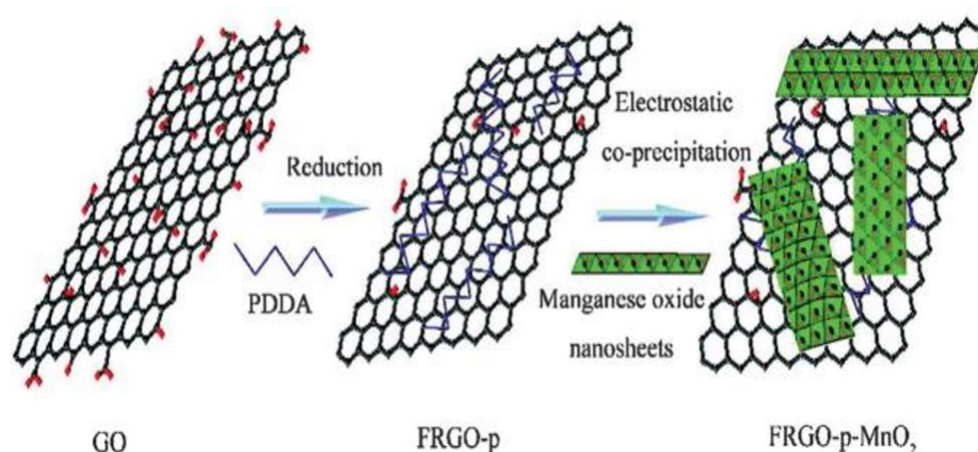


Figure 11. Schematic representation of the assembly process of FRGO-p- MnO_2 . Copyright © 2015 Elsevier Ltd. SMNs were fixed on the surface of rGO self-assembly and the resulting nanocomposites (SMN-RGO) could be used in supercapacitors. As shown in Figure 12a, the rectangular area of the cyclic voltammery (CV) circuit in SmRGO2 (the theoretical mass ratio $\text{Sm}_2\text{O}_3/\text{GO}$ is 1/1) was the largest. The specific capacitance (SC) value of the electrode calculated at a scanning rate of 50 mV/s was 227 F/g, which may have been caused by the synergistic effect between the components. Furthermore, the number of available active sites and the energy that could be stored at the supercapacitor electrode increased [100]. As shown in Figure 12b, the SCs of rGO, Sm_2O_3 , SmRGO1 (the theoretical mass ratio $\text{Sm}_2\text{O}_3/\text{GO}$ is 2/1), SmRGO2, and SmRGO3 (the theoretical mass ratio $\text{Sm}_2\text{O}_3/\text{GO}$ is 1/2) decreased by varying degrees after 4000 cycles. The SC of SmRGO2 showed very high cycle stability, decreasing by 1.0% after 4000 cycles. Therefore, the application of the rGO dosage is very important to improve the cycle stability [100].

A high-density hybrid film was prepared by self-assembly technology. The prepared activated carbon film could be used as the binder-free electrode of a supercapacitor. The constant current charge—discharge curve of the electrode (Figure 12c) showed that it had ideal charge—discharge characteristics and good reversibility [101].

Through the self-assembly of in situ carbon-fiber-coated WO_{3-x} , a DNA-like double helix WO_{3-x} /ultrafine fiber structure (DNA-WC) was designed. As an advanced supercapacitor material, it had excellent electrochemical properties, and its stability was greater than 94% (Figure 12d) after more than 5000 continuous cycles [102]. Stability is one of the important factors in the application of supercapacitors. The above materials have been studied in detail. With energy storage becoming a popular research subject, the application potential of supercapacitors in harsh environments has been deeply explored.

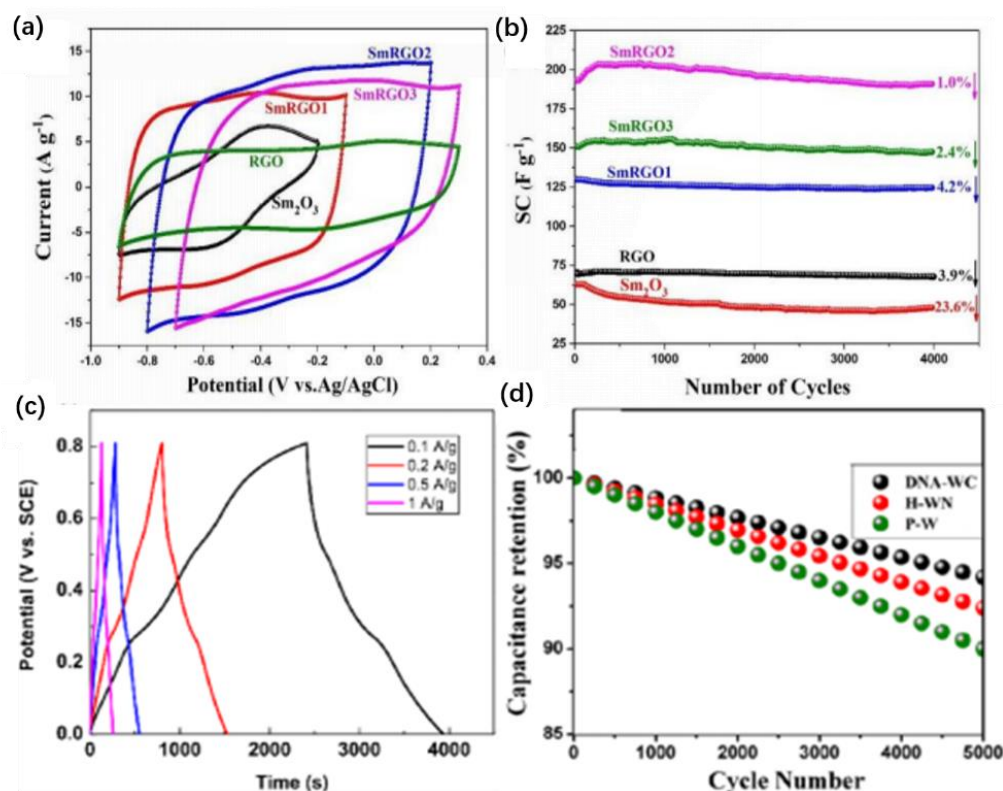


Figure 12. (a) Cyclic voltammograms of Sm_2O_3 nanoparticles SmN and SmN–reduced graphene oxide (SmN-RGO) electrodes with various ratios at 50 mV/s. (b) Specific capacitances of the RGO, SmN, and different SmRGOs as functions of the number of cycles at 200 mV/s. Copyright © 2017 Elsevier B.V. (c) Galvanostatic charge–discharge (GCD) curves of a high-density hybrid $\text{Na}_{0.44}\text{MnO}_2$ nanorod/active carbon films (HNAF) electrode. Copyright© 2021 Springer Nature Switzerland AG. (d) Overlay of cycling stability plots from GCD at a current density of 8 mA/cm². Copyright © 2020 American Chemical Society.

5. Self-Assembled Thin-Film Thermoelectric Materials for Energy Harvesting

5.1. Self-Assembled Thin-Film Thermoelectric Materials for Power Generation Using Waste Heat

As oil and other fossil fuels become increasingly depleted, the development of alternative renewable energy sources to improve energy efficiency is a major theme of current research. Thermoelectric materials can directly convert thermal energy into electrical energy; thus, it is important to develop high-performance thermoelectric films that can convert waste heat directly into electrical energy. Superior thermoelectric materials require high Seebeck coefficients, high electrical conductivities, and low thermal conductivities. Thin-film materials are based on the Seebeck effect and the Peltier effect, allowing for conversion between thermoelectrics with no pollution generated [103]. Gao et al. investigated Sb-doped $\text{Mg}_2(\text{Si}, \text{Sn})$ thermoelectric materials [104]. The results showed that compared to undoped materials, the carrier concentration increased with increasing Sb doping, the power factor showed an increasing trend, and the Seebeck coefficient showed a decreasing trend.

Du et al. studied Sb-doped $\text{Mg}_2\text{Si}_{0.4}\text{Sn}_{0.6}$ materials and reached a consistent conclusion, showing that the Seebeck coefficient increased by about 300 $\mu\text{V}/\text{K}$ [105,106]. The thermoelectric figure of merit for $\text{Mg}_{2.2}\text{Si}_{0.7}\text{Sn}_{0.3}\text{Sb}_{0.01}$ was 0.64 at 723 K. Further studies of Sb-doped Mg_2Si and Mg_2Sn by Liu et al. showed a gradual increase in the Seebeck coefficient, with the thermoelectric figure of merit reaching about 1.3 at 700 K [107].

Polymer-based thermoelectric materials have been widely noticed for their good flexibility and low-density properties. To improve the energy conversion efficiencies of thermoelectric materials, polymer-based composites have become a popular research

topic. Liu et al. prepared a functional film self-assembled from Bi_2Se_3 nanopillars using a solvothermal method [108], and the power factor of thermoelectricity was increased from $1.1 \mu\text{W}/\text{cm}\cdot\text{K}^2$ of the sheet nanoflowers to $1.7 \mu\text{W}/\text{cm}\cdot\text{K}^2$. The structures can significantly improve the performances of organic thermoelectric materials. Cho et al. prepared double-walled nanotubes (DWNT)-polyethyleneimine (PEI)/graphene-PVP multilayer nanocomposites using an LbL assembly method (Figure 13a), which uniformly bound active conducting elements into layered 3D hybrid organic nanostructures, significantly improving the electrical conductivity as well as the Seebeck coefficient (Figure 13b) [109]. Due to the increased conductivity of the nanocomposites, the power factor was also substantially increased, with a power factor of $1.9 \mu\text{W}/\text{cm}\cdot\text{K}^2$. Te-based thermoelectric thin-film materials have attracted widespread interest due to their excellent thermoelectric properties. Zhou et al. prepared Te thin films by electrodeposition on stainless-steel substrates (SSS) with high flexibility. The room temperature power factor was $3.21 \mu\text{W}/\text{cm}\cdot\text{K}^2$ and the thermal conductivity was $4.4 \text{ W}/\text{K}\cdot\text{m}$ [103].

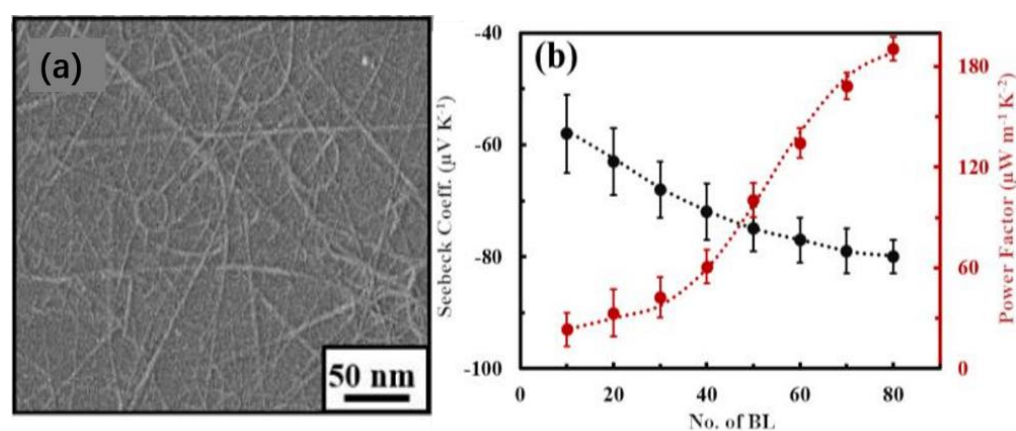


Figure 13. (a) SEM surface image of two bilayers (BL) DWNT-PEI/graphene-polyvinylpyrrolidone (PVP) on Si wafer. (b) Seebeck coefficient and power factor of DWNT-PEI/graphene-PVP. Copyright © 2021 Elsevier B.V.

5.2. Self-Assembled Thin-Film Thermoelectric Materials for Refrigeration Systems

In recent years, nanostructured thin films have been gaining attention in power generation and solid-state cooling due to their various attributes, including their long lifetimes, absence of moving liquids and moving parts, and no toxic gas emissions. To improve the thermoelectric properties of nanostructured thin films, it has been found that factors such as the Seebeck coefficient and the electrical and thermal conductivities need to be controlled [110]. Many studies have been conducted to obtain high non-dimensional performance coefficient (ZT) values, Seebeck coefficients, and electrical conductivities and low thermal conductivities of thin-film thermoelectric materials [111].

The thermoelectric effect was discovered by Thomas John Seebeck in 1821 and was refined by Jean Charles Peltier in 1834 [112]. In the 1950s, the application of the thermoelectric effect to refrigeration gradually garnered attention. The performances of refrigeration systems are mainly determined by the non-dimensional coefficient of merit ZT, and therefore, there is potential for the development of techniques to increase the value of ZT.

Fu et al. prepared nanomaterials by solvothermal synthesis and used them to prepare Bi_2Te_3 nanosheets and Bi_2Te_3 nanoflowers by chemical self-assembly of these nanoplates as building blocks [113]. As shown in Figure 1, the shape of the nanoparticles could be controlled by controlling the amount of ethylenediaminetetraacetic acid (EDTA, 0.01–0.1 g) added during the chemical self-assembly process. As the amount of EDTA added increased [114–116], the nanoparticles formed 3D nanoflowers due to self-assembly, and the nanoflowers disappeared when the amount of added EDTA reached 0.7 g (as shown in Figure 14a–c). The thermoelectric properties of the Bi_2Te_3 nanosheets and Bi_2Te_3 nanoflowers were compared after their preparation. It was found that the thermal conductivity and

resistivity of the nanoflowers were lower than those of the nanosheets, and the Seebeck coefficient of the nanoflowers was higher than that of the nanosheets (Figure 14d–f). The conclusion is that one of the main reasons for the increase in the ZT value to 0.7 is the decrease in the thermal conductivity of the self-assembled synthesized nanoflowers.

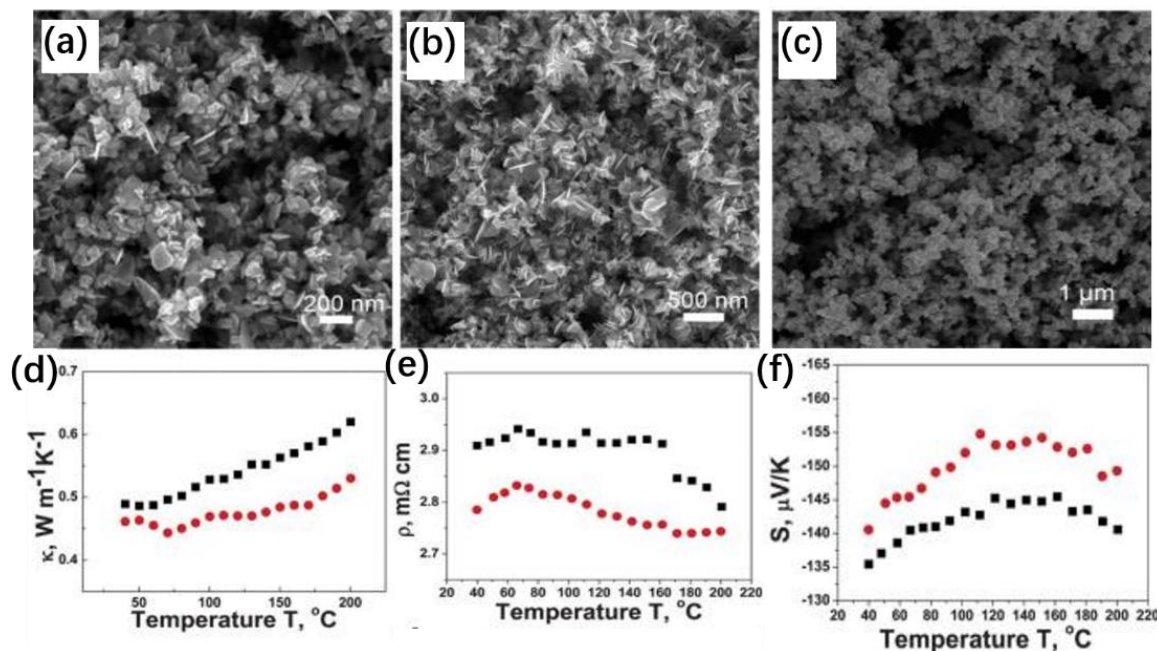


Figure 14. FESEM images of the Bi_2Te_3 products obtained by adding different amounts of ethylenediaminetetraacetic acid (EDTA): (a) 0.01 g, (b) 0.03 g, and (c) 0.07 g. (d) Thermal conductivity, (e) electric resistivity, and (f) thermopower of plate Bi_2Te_3 pellet (squares) and flower Bi_2Te_3 pellet (circles). Copyright © The Royal Society of Chemistry 2012.

Hong et al. prepared mesoporous ZnO films using a low-cost sol–gel method and evaporation-induced self-assembly (EISA) and investigated the effect of the molar ratio of the surfactant/precursor on the hot spot properties of mesoporous ZnO films, including the effect of the surfactant concentration on the Seebeck coefficients, conductivities, and carrier concentrations of the resulting films [111,117]. The films were classified into three different concentrations of 0.03, 0.05, and 0.09 (indexed as Z3, Z5, and Z9 during the annealing process, respectively) based on the molar ratio of surfactant/precursor for the analysis of the thermoelectric properties. First, to remove the surfactant from the mesoporous ZnO films, the films were annealed at 450 °C under a vacuum, and the Fourier transform infrared spectroscopy spectra before and after annealing were compared. The organic bonds in Z3 and Z9 disappeared (Figure 15a), indicating that the surfactant was removed after low-temperature annealing. With the removal of the surfactant, the improvement of the thermoelectric properties of the mesoporous ZnO films was analyzed as follows: the porosity of the films increased from 29% to 40% with the increase in the surfactant concentration (Figure 15b), and the gradual increase in the porosity indicated that the concentration of carriers decreased with the increase in the surfactant concentration (Figure 15d). As shown in Figure 2c, the Seebeck coefficient increased with increasing surfactant/precursor molar ratio. The Seebeck coefficients of the mesoporous ZnO films were inversely proportional to the carrier concentration. However, the Seebeck coefficient was not the only factor that affected the thermoelectric properties of the films; high electrical conductivity and low thermal conductivity were also required. As shown in Figure 15e, the conductivity of the mesoporous ZnO films decreased with increasing surfactant/precursor molar ratio, but the decrease was weak relative to the increase in the Seebeck coefficient, i.e., the higher the surfactant/precursor molar ratio was, the better the thermoelectric properties of mesoporous ZnO films became.

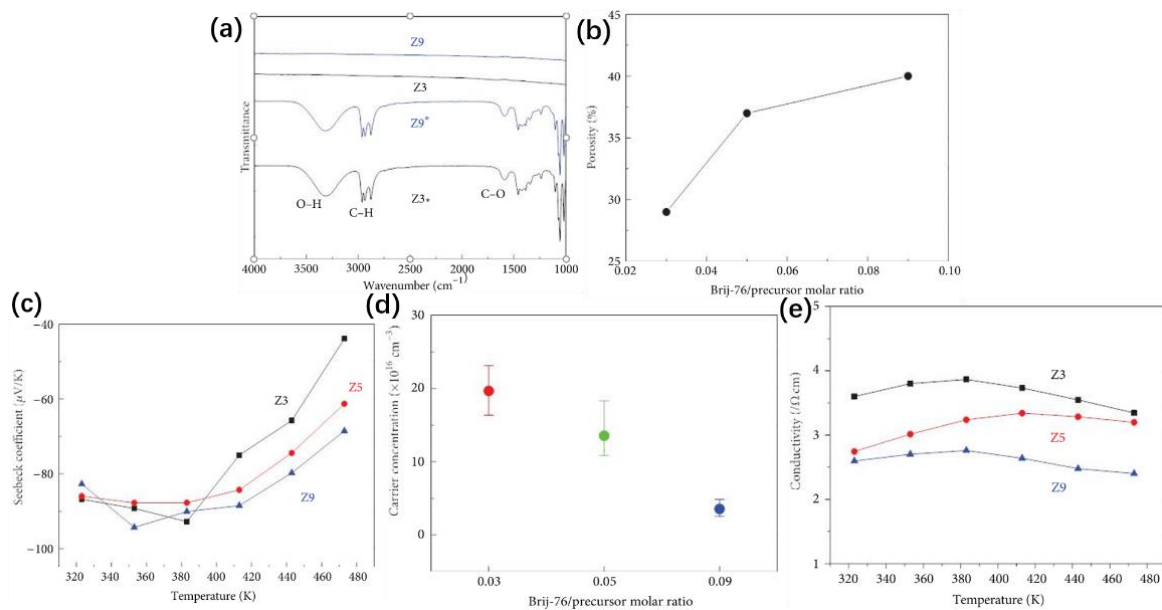


Figure 15. (a) Fourier transform infrared spectroscopy spectra of mesoporous ZnO thin films produced using various surfactant concentrations before annealing (Z3* and Z9*) and after annealing (Z3 and Z9) at 450 °C. (b) Porosity, (c) Seebeck coefficient, (d) carrier concentration, and (e) electrical conductivity changes in mesoporous ZnO thin films synthesized using various surfactant concentrations. Copyright © 2013 Min-Hee Hong.

6. Conclusions and Perspectives

From the review above, it is evident that there are many interesting examples and new developments related to self-assembled nanocomposites and nanostructures. Their superior properties make them suitable for environmental and energetic applications. In addition to the self-assembly approach, significant progress has also been achieved in the fabrication of new self-assembled nanocomposites that enable the combination of the advantages of self-assembled nanostructures and applications, in which the advantages of the self-assembled nanocomposites can be exploited. This review outlined the achievements of self-assembled powders and membrane nanocatalysts for wastewater purification and hydrogen production from water, as well as self-assembled nanocomposites for lithium-ion batteries, supercapacitors, and energy harvesting. More attention should be paid to energy harvesting, including self-assembled thin-film thermoelectric materials for power generation and refrigerating systems, which are industrially significant.

Great progress has been achieved in both the fabrication and application of self-assembled nanocomposites and nanostructures. From an application perspective, even though a variety of self-assembled architectures have been developed, many questions remain. For example, self-assembled nanostructures could potentially serve as potential materials, something which has not been realized yet. It has also been predicted that the full development of fabrication strategies could be readily incorporated into the design and preparation of novel functional materials and devices. New environmentally friendly sources and energetic optimization are important for society. Self-assembled materials could help to bridge fundamental research and practical applications and open the door to a new generation of functional materials. We believe that this mini-review has great potential for the development of environmental and energy applications, and self-assembled materials with improved features should continue to be perfected to achieve better performances.

Author Contributions: Writing—review and editing, S.C., X.W., Q.H., X.S., A.W., X.D., L.S. and Y.Z.; editing and supervision, Q.S. and S.C. All authors have read and agreed to the published version of the manuscript.

Funding: This research was financially supported by the 2018 Doctoral Research Funds of Shandong Jianzhu University (X18064Z), Joint Fund Project for Natural Science Foundation of Shandong Province (ZR2019LLZ002), and the National Nature Science Foundation of China (Grant No. 52002225).

Institutional Review Board Statement: Not applicable.

Informed Consent Statement: Not applicable.

Data Availability Statement: Not applicable.

Conflicts of Interest: The authors declare no conflict of interest.

References

1. Grzybowski, B.A.; Wilmer, C.E.; Kim, J.; Browne, K.P.; Bishop, K.J.M. Self-assembly: From crystals to cells. *Soft Matter* **2009**, *5*, 1110–1128. [[CrossRef](#)]
2. Grzelczak, M.; Vermant, J.; Furst, E.M.; Liz-Marzán, L.M. Directed Self-Assembly of Nanoparticles. *ACS Nano* **2010**, *4*, 3591–3605. [[CrossRef](#)] [[PubMed](#)]
3. Joshi, A.; Singh, N.; Verma, G. Chapter 2—Preparation and applications of self-assembled natural and synthetic nanostructures. In *Fabrication and Self-Assembly of Nanobiomaterials*; Grumezescu, A.M., Ed.; William Andrew Publishing: Norwich, NY, USA, 2016; pp. 29–55.
4. Lin, Y.; Böker, A.; He, J.; Sill, K.; Xiang, H.; Abetz, C.; Li, X.; Wang, J.; Emrick, T.; Long, S.; et al. Self-directed self-assembly of nanoparticle/copolymer mixtures. *Nature* **2005**, *434*, 55–59. [[CrossRef](#)] [[PubMed](#)]
5. Thorkelsson, K.; Bai, P.; Xu, T. Self-assembly and applications of anisotropic nanomaterials: A review. *Nano Today* **2015**, *10*, 48–66. [[CrossRef](#)]
6. Maeda, K.; Domen, K. Surface Nanostructures in Photocatalysts for Visible-Light-Driven Water Splitting. *Photocatalysis* **2011**, *303*, 95–119.
7. Reddy, A.L.M.; Gowda, S.R.; Shaijumon, M.M.; Ajayan, P.M. Hybrid Nanostructures for Energy Storage Applications. *Adv. Mater.* **2012**, *24*, 5045–5064. [[CrossRef](#)]
8. Klinkova, A.; Choueiri, R.M.; Kumacheva, E. Self-assembled plasmonic nanostructures. *Chem. Soc. Rev.* **2014**, *43*, 3976–3991. [[CrossRef](#)]
9. Howard, R.E.; Skocpol, W.J.; Jackel, L.D. Nanostructures. *Annu. Rev. Mater. Sci.* **1986**, *16*, 441–466. [[CrossRef](#)]
10. Yazdani, S.; Pettes, M.T. Nanoscale self-assembly of thermoelectric materials: A review of chemistry-based approaches. *Nanotechnology* **2018**, *29*, 432001. [[CrossRef](#)]
11. Pomerantseva, E.; Bonaccorso, F.; Feng, X.; Cui, Y.; Gogotsi, Y. Energy storage: The future enabled by nanomaterials. *Science* **2019**, *366*, eaan8285. [[CrossRef](#)]
12. Fitriani; Ovik, R.; Long, B.D.; Barma, M.C.; Riaz, M.; Sabri, M.F.M.; Said, S.M.; Saidur, R. A review on nanostructures of high-temperature thermoelectric materials for waste heat recovery. *Renew. Sustain. Energy Rev.* **2016**, *64*, 635–659. [[CrossRef](#)]
13. Qin, X.; Wang, J.; Zhang, Y.; Wang, Z.; Li, S.; Zhao, S.; Matyjaszewski, K. Self-Assembly Strategy for Double Network Elastomer Nanocomposites with Ultralow Energy Consumption and Ultrahigh Wear Resistance. *Adv. Funct. Mater.* **2020**, *30*, 2003429. [[CrossRef](#)]
14. Wang, D.; Kou, R.; Choi, D.; Yang, Z.; Nie, Z.; Li, J.; Aksay, I.A. Ternary self-assembly of ordered metal oxide- graphene nanocomposites for electrochemical energy storage. *ACS Nano* **2010**, *4*, 1587–1595. [[CrossRef](#)]
15. Zhao, K.; Peng, W.; Holder, K. Agafonov, Alexanderonmental applications. *ACS Sustain. Chem. Eng.* **2016**, *4*, 2814–2821.
16. Sefhra, P.J.; Baraneedharan, P.; Sivakumar, M.; Thangadurai, T.D.; Nehru, K. Size controlled synthesis of SnO₂ and its electrostatic self-assembly over reduced graphene oxide for photocatalyst and supercapacitor application. *Mater. Res. Bull.* **2018**, *106*, 103–112. [[CrossRef](#)]
17. Costantini, A.; Venezia, V.; Pota, G.; Bifulco, A.; Califano, V.; Sannino, F. Adsorption of cellulase on wrinkled silica nanoparticles with enhanced inter-wrinkle distance. *Nanomaterials* **2020**, *10*, 1799. [[CrossRef](#)] [[PubMed](#)]
18. Garnweitner, G.; Smarsly, B.; Assink, R.; Ruland, W.; Bond, E.; Brinker, C.J. Self-assembly of an environmentally responsive polymer/silica nanocomposite. *J. Am. Chem. Soc.* **2003**, *125*, 5626–5627. [[CrossRef](#)]
19. Fujishima, A.; Honda, K. Electrochemical Photolysis of Water at a Semiconductor Electrode. *Nature* **1972**, *238*, 37–38. [[CrossRef](#)]
20. Patil, S.B.; Basavarajappa, P.S.; Ganganagappa, N.; Jyothi, M.S.; Raghu, A.V.; Reddy, K.R. Recent advances in non-metals-doped TiO₂ nanostructured photocatalysts for visible-light driven hydrogen production, CO₂ reduction and air purification. *Int. J. Hydrogen Energy* **2019**, *44*, 13022–13039. [[CrossRef](#)]
21. EL-Mekkawi, D.M.; Abdelwahab, N.A.; Mohamed, W.A.; Taha, N.A.; Abdel-Mottaleb, M.S.A. Solar photocatalytic treatment of industrial wastewater utilizing recycled polymeric disposals as TiO₂ supports. *J. Clean. Prod.* **2020**, *249*, 119430. [[CrossRef](#)]
22. Shu, Y.; Huang, R.; Wei, X.; Liu, L.; Jia, Z. Pb(II) Removal Using TiO₂-Embedded Monolith Composite Cryogel as an Alternative Wastewater Treatment Method. *Water Air Soil Pollut.* **2017**, *228*, 375.1–375.16. [[CrossRef](#)]
23. Wang, L.; Ali, J.; Zhang, C.; Mailhot, G.; Pan, G. Simultaneously enhanced photocatalytic and antibacterial activities of TiO₂/Ag composite nanofibers for wastewater purification. *J. Environ. Chem. Eng.* **2020**, *8*, 102104. [[CrossRef](#)]

24. Chen, H.; Benedek, P.; Fisher, K.-J.; Wood, V.; Cui, Y. Self-Assembled materials for electrochemical energy storage. *MRS Bull.* **2020**, *45*, 815–822. [[CrossRef](#)]
25. Hu, C.; Miao, L.; Yang, Q.; Yu, X.; Song, L.; Zheng, Y.; Wang, C.; Li, L.; Zhu, L.; Cao, X.; et al. Self-assembly of CNTs on Ni foam for enhanced performance of NiCoO₂@CNT@NF supercapacitor electrode. *Chem. Eng. J.* **2021**, *410*, 128317. [[CrossRef](#)]
26. Wei, X.; Wan, S.; Gao, S. Self-assembly-template engineering nitrogen-doped carbon aerogels for high-rate supercapacitors. *Nano Energy* **2016**, *28*, 206–215. [[CrossRef](#)]
27. Peng, Q.; Peng, G.; Wu, L.; Wang, X.; Wang, N.; Li, X. Influence of TiO₂ crystallinity on TiO₂ nanotube confined CdS nanoparticles for photocatalytic hydrogen production. *Inorg. Nano-Met. Chem.* **2020**, *50*, 599–605. [[CrossRef](#)]
28. Yendrapati, T.P.; Gautam, A.; Bojja, S.; Pal, U. Formation of ZnO@CuS nanorods for efficient photocatalytic hydrogen generation. *Sol. Energy* **2020**, *196*, 540–548. [[CrossRef](#)]
29. Liu, X.; Li, J.; Yao, W. CdS@MoS₂ Hetero-structured Nanocomposites Are Highly Effective Photo-Catalysts for Organic Dye Degradation. *ACS Omega* **2020**, *5*, 27463–27469. [[CrossRef](#)]
30. Yin, J.; Ge, B.; Jiao, T.; Qin, Z.; Yu, M.; Zhang, L.; Zhang, Q.; Peng, Q. Self-Assembled Sandwich-like MXene-Derived Composites as Highly Efficient and Sustainable Catalysts for Wastewater Treatment. *Langmuir* **2021**, *37*, 1267–1278. [[CrossRef](#)]
31. Ali, W.; Ullah, H.; Zada, A.; Muhammad, W.; Ali, S.; Shaheen, S.; Alamgir, M.K.; Ansar, M.Z.; Khan, Z.U.; Bilal, H. Synthesis of TiO₂ modified self-assembled honeycomb ZnO/SnO₂ nanocomposites for exceptional photocatalytic degradation of 2, 4-dichlorophenol and bisphenol A. *Sci. Total Environ.* **2020**, *746*, 141291. [[CrossRef](#)]
32. Liu, Y.; Xu, C.; Zhu, Z.; Lu, J.; Manohari, A.G.; Shi, Z. Self-assembled ZnO/Ag hollow spheres for effective photocatalysis and bacteriostasis. *Mater. Res. Bull.* **2018**, *98*, 64–69. [[CrossRef](#)]
33. Yuan, R.; Qiu, J.; Yue, C.; Shen, C.; Li, D.; Zhu, C.; Liu, F.; Li, A. Self-assembled hierarchical and bifunctional MIL-88A (Fe)@ZnIn₂S₄ heterostructure as a reusable sunlight-driven photocatalyst for highly efficient water purification. *Chem. Eng. J.* **2020**, *401*, 126020. [[CrossRef](#)]
34. Mahlambi, M.M.; Ngila, C.J.; Mamba, B.B. Recent Developments in Environmental Photocatalytic Degradation of Organic Pollutants: The Case of Titanium Dioxide Nanoparticles—A Review. *J. Nanomater.* **2015**, *2015*, 790173. [[CrossRef](#)]
35. Ma, D.; Yi, H.; Lai, C.; Liu, X.; Huo, X.; An, Z.; Li, L.; Fu, Y.; Li, B.; Zhang, M.; et al. Critical review of advanced oxidation processes in organic wastewater treatment. *Chemosphere* **2021**, *275*, 130104. [[CrossRef](#)] [[PubMed](#)]
36. Ikram, D.M.; Rashid, M.; Haider, A.; Naz, S.; Haider, J.; Raza, A.; Ansar, M.; Uddin, M.; Ali, N.; Ahemd, D.S.; et al. A review of photocatalytic characterization, and environmental cleaning, of metal oxide nanostructured materials. *Sustain. Mater. Technol.* **2021**, *30*, e00343. [[CrossRef](#)]
37. Sun, X.; Lu, J.; Wu, J.; Guan, D.; Liu, Q.; Yan, N. Enhancing Photocatalytic Activity on Gas-phase Heavy Metal Oxidation with Self-assembled BiOI/BiOCl Microflowers. *J. Colloid. Interf. Sci.* **2019**, *546*, 32–42. [[CrossRef](#)] [[PubMed](#)]
38. Patel, H.K.; Kalaria, R.K.; Khimani, M.R. 20—Nanotechnology: A promising tool for Bioremediation. In *Removal of Toxic Pollutants Through Microbiological and Tertiary Treatment*; Shah, M.P., Ed.; Elsevier: Amsterdam, The Netherlands, 2020; pp. 515–547.
39. Guerra, F.D.; Attia, M.F.; Whitehead, D.C.; Alexis, F. Nanotechnology for Environmental Remediation: Materials and Applications. *Molecules* **2018**, *23*, 1760. [[CrossRef](#)]
40. González-González, R.B.; Sharma, A.; Parra-Saldívar, R.; Ramirez-Mendoza, R.A.; Bilal, M.; Iqbal, H.M.N. Decontamination of emerging pharmaceutical pollutants using carbon-dots as robust materials. *J. Hazard. Mater.* **2022**, *423*, 127145. [[CrossRef](#)]
41. Deshpande, B.D.; Agrawal, P.S.; Yenkie, M.K.N.; Dhoble, S.J. Prospective of nanotechnology in degradation of waste water: A new challenges. *Nano-Struct. Nano-Objects* **2020**, *22*, 100442. [[CrossRef](#)]
42. Rego, R.M.; Kuriya, G.; Kurkuri, M.D.; Kigga, M. MOF based engineered materials in water remediation: Recent trends. *J. Hazard. Mater.* **2021**, *403*, 123605. [[CrossRef](#)]
43. Nakate, U.T.; Singh, V.K.; Yu, Y.T.; Park, S. WO₃ nanorods structures for high-performance gas sensing application. *Mater. Lett* **2021**, *299*, 130092. [[CrossRef](#)]
44. Wu, D.; Liu, H.; Chen, J.; Liu, W.; Histan, G.; Wang, T. Cu NPs-embedded cross-linked microporous 3D reduced graphene hydrogels as photocatalyst for hydrogen evolution. *J. Colloid Interface Sci.* **2020**, *577*, 441–449. [[CrossRef](#)] [[PubMed](#)]
45. Kerkez, D.; Bečelić-Tomin, M.; Gvoić, V.; Dalmacija, B. Metal Nanoparticles in Dye Wastewater Treatment—Smart Solution for Clear Water. *Recent Pat. Nanotechnol.* **2021**, *15*, 270–294. [[CrossRef](#)]
46. Madea, M. Effect of copper nanoparticles on biological wastewater treatment. *Desalination Water Treat.* **2020**, *199*, 493–498. [[CrossRef](#)]
47. Das, C.; Sen, S.; Singh, T.; Ghosh, T.; Paul, S.S.; Kim, T.W.; Jeon, S.; Maiti, D.K.; Im, J.; Biswas, G. Green Synthesis, Characterization and Application of Natural Product Coated Magnetite. *Nanopart. Wastewater Treat.* **2020**, *10*, 1615.
48. Wang, R.; Cai, C.; Wang, D.; Liu, Z.; Gao, L.; Jiao, T. Self-assembled Au/Fe₃O₄ nanoparticle-loaded phytic acid-graphene oxide composite foam with highly efficient catalytic performance for p-nitrophenol and o-nitroaniline organic pollutants. *Colloids Surf. A Physicochem. Eng. Asp.* **2021**, *617*, 126368. [[CrossRef](#)]
49. Qian, C.; Yin, J.; Zhao, J.; Li, X.; Wang, S.; Bai, Z.; Jiao, T. Facile preparation and highly efficient photodegradation performances of self-assembled Artemia eggshell-ZnO nanocomposites for wastewater treatment. *Colloids Surf. A Physicochem. Eng. Asp.* **2021**, *610*, 125752. [[CrossRef](#)]

50. Liu, Y.; Hou, C.; Jiao, T.; Song, J.; Zhang, X.; Xing, R.; Zhou, J.; Zhang, L.; Peng, Q. Self-Assembled AgNP-Containing Nanocomposites Constructed by Electrospinning as Efficient Dye Photocatalyst Materials for Wastewater Treatment. *Nanomaterials* **2018**, *8*, 35. [[CrossRef](#)]
51. Ding, J.; Li, X.; Chen, L.; Zhang, X.; Tian, X. Photocatalytic hydrogen production over plasmonic AuCu/CaIn₂S₄ composites with different AuCu atomic arrangements. *Appl. Catal. B Environ.* **2018**, *224*, 322–329. [[CrossRef](#)]
52. Yang, C.; Yu, M.; Cao, X.; Bian, X. Application of Amorphous Nanoparticle Fe-B Magnetic Fluid in Wastewater Treatment. *Nano* **2019**, *14*, 1950119. [[CrossRef](#)]
53. Maeda, K.; Xiong, A.; Yoshinaga, T.; Ikeda, T.; Sakamoto, N.; Hisatomi, T.; Takashima, M.; Lu, D.; Kanehara, M.; Setoyama, T.; et al. Photocatalytic Overall Water Splitting Promoted by Two Different Cocatalysts for Hydrogen and Oxygen Evolution under Visible Light. *Angew. Chem. Int. Ed.* **2010**, *49*, 4096–4099. [[CrossRef](#)] [[PubMed](#)]
54. Sharma, H.; Dhir, A. Hydrogen augmentation of biogas through dry reforming over bimetallic nickel-cobalt catalysts supported on titania. *Fuel* **2020**, *279*, 118389. [[CrossRef](#)]
55. Stamenkovic, V.R.; Mun, B.S.; Arenz, M.; Mayrhofer, K.J.J.; Lucas, C.A.; Wang, G.; Ross, P.N.; Markovic, N.M. Trends in electrocatalysis on extended and nanoscale Pt-bimetallic alloy surfaces. *Nat. Mater.* **2007**, *6*, 241–247. [[CrossRef](#)] [[PubMed](#)]
56. Fane, A.G.; Wang, R.; Hu, M.X. Synthetic Membranes for Water Purification: Status and Future. *Angew. Chem. Int. Ed.* **2015**, *54*, 3368–3386. [[CrossRef](#)]
57. Bai, H.; Sun, D.D. Hybrid TiO₂ photocatalytic oxidation and ultrafiltration for humic acid removal and membrane fouling control. *Water Supply* **2011**, *11*, 324–332. [[CrossRef](#)]
58. Liu, Y.; Xue, J.; Duan, Y.; Qiang, L.; Ma, J. Layer-by-layer Self-assembly Polyurethane/TiO₂ NPs Hybrid Film and Its Photocatalytic Efficiency for Decolorization of Methyl Blue. *Fibers Polym.* **2019**, *20*, 1833–1840. [[CrossRef](#)]
59. Zhang, Q.; Wang, H.; Fan, X.; Lv, F.; Chen, S.; Quan, X. Fabrication of TiO₂ nanofiber membranes by a simple dip-coating technique for water treatment. *Surf. Coat. Technol.* **2016**, *298*, 45–52. [[CrossRef](#)]
60. Bai, H.; Zan, X.; Zhang, L.; Sun, D.D. Multi-functional CNT/ZnO/TiO₂ nanocomposite membrane for concurrent filtration and photocatalytic degradation. *Sep. Purif. Technol.* **2015**, *156*, 922–930. [[CrossRef](#)]
61. Chang, S.; Wang, Q.; Liu, B.; Sang, Y.; Liu, H. Hierarchical TiO₂ nanonetwork-porous Ti 3D hybrid photocatalysts for continuous-flow photoelectrodegradation of organic pollutants. *Catal. Sci. Technol.* **2017**, *7*, 524–532. [[CrossRef](#)]
62. He, J.; Zhang, Y.; Zhang, X.; Huang, Y. Highly efficient Fenton and enzyme-mimetic activities of NH₂-MIL-88B(Fe) metal organic framework for methylene blue degradation. *Sci. Rep.* **2018**, *8*, 5159. [[CrossRef](#)]
63. Gao, L.; Zhuang, J.; Nie, L.; Zhang, J.; Zhang, Y.; Gu, N.; Wang, T.; Feng, J.; Yang, D.; Perrett, S.; et al. Intrinsic peroxidase-like activity of ferromagnetic nanoparticles. *Nat. Nanotechnol.* **2007**, *2*, 577–583. [[CrossRef](#)] [[PubMed](#)]
64. Wang, Y.; Zhao, M.; Hou, C.; Yang, X.; Li, Z.; Meng, Q.; Liang, C. Graphene-based magnetic metal organic framework nanocomposite for sensitive colorimetric detection and facile degradation of phenol. *J. Taiwan Inst. Chem. Eng.* **2019**, *102*, 312–320. [[CrossRef](#)]
65. Brillas, E.; Sirés, I.; Oturan, M.A. Electro-Fenton Process and Related Electrochemical Technologies Based on Fenton's Reaction Chemistry. *Chem. Rev.* **2009**, *109*, 6570–6631. [[CrossRef](#)] [[PubMed](#)]
66. Niu, H.; Zheng, Y.; Wang, S.; Zhao, L.; Yang, S.; Cai, Y. Continuous generation of hydroxyl radicals for highly efficient elimination of chlorophenols and phenols catalyzed by heterogeneous Fenton-like catalysts yolk/shell Pd@Fe₃O₄@metal organic frameworks. *J. Hazard. Mater.* **2018**, *346*, 174–183. [[CrossRef](#)] [[PubMed](#)]
67. Mousavi, M.; Habibi-Yangjeh, A.; Seifzadeh, D. Novel ternary g-C₃N₄/Fe₃O₄/MnWO₄ nanocomposites: Synthesis, characterization, and visible-light photocatalytic performance for environmental purposes. *J. Mater. Sci. Technol.* **2018**, *34*, 1638–1651. [[CrossRef](#)]
68. Ran, J.; Ma, T.Y.; Gao, G.; Du, X.-W.; Qiao, S.Z. Porous P-doped graphitic carbon nitride nanosheets for synergistically enhanced visible-light photocatalytic H₂ production. *Energy Environ. Sci.* **2015**, *8*, 3708–3717. [[CrossRef](#)]
69. Zhou, L.; Liu, D.; Wang, J.; Wang, Z.L. Triboelectric nanogenerators: Fundamental physics and potential applications. *Friction* **2020**, *8*, 481–506. [[CrossRef](#)]
70. Dal'Acqua, N.; Scheffer, F.R.; Boniatti, R.; da Silva, B.V.M.; de Melo, J.V.; da Silva Crespo, J.; Giovanela, M.; Pereira, M.B.; Weibel, D.E.; Machado, G. Photocatalytic Nanostructured Self-Assembled Poly(allylamine hydrochloride)/Poly(acrylic acid) Polyelectrolyte Films Containing Titanium Dioxide-Gold Nanoparticles for Hydrogen Generation. *J. Phys. Chem. C* **2013**, *117*, 23235–23243. [[CrossRef](#)]
71. He, G.; Wen, Y.; Ma, C.; Li, X.; Wang, L.; Gao, L.; Sun, Z. Nanoporous CoFe₂O₄ Loaded with Pt-Ag for Photocatalytic Hydrogen Evolution. *JOM* **2021**, *73*, 2798–2807. [[CrossRef](#)]
72. Qi, K.; Yu, J. Chapter 8—Modification of ZnO-based photocatalysts for enhanced photocatalytic activity. In *Interface Science and Technology*; Yu, J., Jaroniec, M., Jiang, C., Eds.; Elsevier: Amsterdam, The Netherlands, 2020; Volume 31, pp. 265–284.
73. Jin, Z.; Gong, H.; Li, H. Visible-light-driven two dimensional metal-organic framework modified manganese cadmium sulfide for efficient photocatalytic hydrogen evolution. *J. Colloid Interface Sci.* **2021**, *603*, 344–355. [[CrossRef](#)]
74. Zhang, J.; Yang, L.; Cui, Y.; Tang, Y.L.; Xu, J.Y.; Su, Z.C.; Lao, X.Z.; Bao, Y.T.; Wang, X.R.; Xu, S.J. The role of luminescence self-absorption in photocatalytic properties of self-assembled ZnS nanocrystals. *AIP Adv.* **2020**, *10*, 105314. [[CrossRef](#)]
75. Bhirud, A.; Chaudhari, N.; Nikam, L.; Sonawane, R.; Patil, K.; Baeg, J.-O.; Kale, B. Surfactant tunable hierarchical nanostructures of CdIn₂S₄ and their photohydrogen production under solar light. *Int. J. Hydrogen Energy* **2011**, *36*, 11628–11639. [[CrossRef](#)]

76. Zhou, Y. Nanostructured Thin Film Electrode Materials for Lithium Ion Battery. *Prog. Chem.* **2011**, *23*, 336–348.
77. Li, C.; Xu, X.; Song, T.; Zhu, X.; Li, Y.; Jia, H.; Liu, Y. Fabrication of GeS-graphene composites for electrode materials in lithium-ion batteries. *Mater. Res. Express* **2021**, *8*, 115013. [[CrossRef](#)]
78. Poizot, P.; Baudrin, E.; Laruelle, S.; Dupont, L.; Touboul, M.; Tarascon, J.M. Low temperature synthesis and electrochemical performance of crystallized $\text{FeVO}_4 \cdot 1.1\text{H}_2\text{O}$. *Solid State Ion.* **2000**, *138*, 31–40. [[CrossRef](#)]
79. Zhang, W.; Cao, P.; Li, L.; Yang, K.; Wang, K.; Liu, S.; Yu, Z. Carbon-encapsulated 1D SnO_2/NiO heterojunction hollow nanotubes as high-performance anodes for sodium-ion batteries. *Chem. Eng. J.* **2018**, *348*, 599–607. [[CrossRef](#)]
80. Böhme, S.; Philippe, B.; Edström, K.; Nyholm, L. Photoelectron Spectroscopic Evidence for Overlapping Redox Reactions for SnO_2 Electrodes in Lithium-Ion Batteries. *J. Phys. Chem. C* **2017**, *121*, 4924–4936. [[CrossRef](#)]
81. Wang, H.; Cui, L.-F.; Yang, Y.; Sanchez Casalongue, H.; Robinson, J.T.; Liang, Y.; Cui, Y.; Dai, H. Mn_3O_4 –Graphene Hybrid as a High-Capacity Anode Material for Lithium Ion Batteries. *J. Am. Chem. Soc.* **2010**, *132*, 13978–13980. [[CrossRef](#)]
82. Piao, Y.; Kim, H.S.; Sung, Y.-E.; Hyeon, T. Facile scalable synthesis of magnetite nanocrystals embedded in carbon matrix as superior anode materials for lithium-ion batteries. *Chem. Commun.* **2010**, *46*, 118–120. [[CrossRef](#)]
83. Deng, Z.; Peng, B.; Chen, D.; Tang, F.; Muscat, A.J. A New Route to Self-Assembled Tin Dioxide Nanospheres: Fabrication and Characterization. *Langmuir* **2008**, *24*, 11089–11095. [[CrossRef](#)]
84. Man, J.; Liu, K.; Du, Y.; Sun, J. Self-assemble SnO_2 porous nanotubes as high-performance anodes for lithium-ion batteries. *Mater. Chem. Phys.* **2020**, *256*, 123669. [[CrossRef](#)]
85. Chang, K.; Chen, W. In situ synthesis of MoS_2 /graphene nanosheet composites with extraordinarily high electrochemical performance for lithium ion batteries. *Chem. Commun.* **2011**, *47*, 4252–4254. [[CrossRef](#)] [[PubMed](#)]
86. Guo, J.; Chen, X.; Jin, S.; Zhang, M.; Liang, C. Synthesis of graphene-like MoS_2 nanowall/graphene nanosheet hybrid materials with high lithium storage performance. *Catal. Today* **2015**, *246*, 165–171. [[CrossRef](#)]
87. Das, S.K.; Mallavajula, R.; Jayaprakash, N.; Archer, L.A. Self-assembled MoS_2 –carbon nanostructures: Influence of nanostructuring and carbon on lithium battery performance. *J. Mater. Chem.* **2012**, *22*, 12988–12992. [[CrossRef](#)]
88. Wang, X.; Zhou, X.; Yao, K.; Zhang, J.; Liu, Z. A SnO_2 /graphene composite as a high stability electrode for lithium ion batteries. *Carbon* **2011**, *49*, 133–139. [[CrossRef](#)]
89. Sun, Y.; Hu, X.; Luo, W.; Huang, Y. Self-Assembled Hierarchical MoO_2 /Graphene Nanoarchitectures and Their Application as a High-Performance Anode Material for Lithium-Ion Batteries. *ACS Nano* **2011**, *5*, 7100–7107. [[CrossRef](#)]
90. Zheng, F.; Zhu, D.; Shi, X.; Chen, Q. Metal–organic framework-derived porous $\text{Mn}_{1.8}\text{Fe}_{1.2}\text{O}_4$ nanocubes with an interconnected channel structure as high-performance anodes for lithium ion batteries. *J. Mater. Chem. A* **2015**, *3*, 2815–2824. [[CrossRef](#)]
91. Hu, L.; Chen, Q. Hollow/porous nanostructures derived from nanoscale metal–organic frameworks towards high performance anodes for lithium-ion batteries. *Nanoscale* **2014**, *6*, 1236–1257. [[CrossRef](#)]
92. Zhu, D.; Zheng, F.; Xu, S.; Zhang, Y.; Chen, Q. MOF-derived self-assembled $\text{ZnO}/\text{Co}_3\text{O}_4$ nanocomposite clusters as high-performance anodes for lithium-ion batteries. *Dalton Trans.* **2015**, *44*, 16946–16952. [[CrossRef](#)]
93. Xiang, Y.; Lu, S.; Jiang, S.P. Layer-by-layer self-assembly in the development of electrochemical energy conversion and storage devices from fuel cells to supercapacitors. *Chem. Soc. Rev.* **2012**, *41*, 7291–7321. [[CrossRef](#)]
94. Winter, M.; Brodd, R.J. What Are Batteries, Fuel Cells, and Supercapacitors? *Chem. Rev.* **2004**, *104*, 4245–4270. [[CrossRef](#)] [[PubMed](#)]
95. Guo, Y.-G.; Hu, J.-S.; Wan, L.-J. Nanostructured Materials for Electrochemical Energy Conversion and Storage Devices. *Adv. Mater.* **2008**, *20*, 2878–2887. [[CrossRef](#)]
96. Nakate, U.T.; Patil, P.; Choudhury, S.P.; Kale, S.N. Microwave assisted synthesis of Co_3O_4 and NiO nanoplates and structural, optical, magnetic characterizations. *Nano-Struct. Nano-Objects* **2018**, *14*, 66–72. [[CrossRef](#)]
97. Cui, X.; Lv, R.; Sagar, R.U.R.; Liu, C.; Zhang, Z. Reduced graphene oxide/carbon nanotube hybrid film as high performance negative electrode for supercapacitor. *Electrochim. Acta* **2015**, *169*, 342–350. [[CrossRef](#)]
98. Guo, C.X.; Li, C.M. A self-assembled hierarchical nanostructure comprising carbon spheres and graphene nanosheets for enhanced supercapacitor performance. *Energy Environ. Sci.* **2011**, *4*, 4504–4507. [[CrossRef](#)]
99. Hu, C.; Han, Q.; Fei, Z. Graphitic C_3N_4 -Pt nanohybrids supported on a graphene network for highly efficient methanol oxidation. *Sci. China Mater.* **2015**, *58*, 21. [[CrossRef](#)]
100. Dezfouli, A.S.; Ganjali, M.R.; Naderi, H.R. Anchoring samarium oxide nanoparticles on reduced graphene oxide for high-performance supercapacitor. *Appl. Surf. Sci.* **2017**, *402*, 245–253. [[CrossRef](#)]
101. Liu, C.; Huang, S.; Zhao, K.; Xiong, S.; Xu, W.; Zhang, S. Ethanol interfacial assembly of $\text{Na}_{0.44}\text{MnO}_2$ nanorod/active carbon toward the fabrication of high-density hybrid films for binder-free supercapacitor electrode. *J. Nanopart. Res.* **2019**, *21*, 128. [[CrossRef](#)]
102. Salkar, A.V.; Naik, A.P.; Bhosale, S.V.; Morajkar, P.P. Designing a Rare DNA-Like Double Helical Microfiber Superstructure via Self-Assembly of In Situ Carbon Fiber-Encapsulated WO_{3-x} Nanorods as an Advanced Supercapacitor Material. *ACS Appl. Mater. Interfaces* **2021**, *13*, 1288–1300. [[CrossRef](#)]
103. Zhou, J.; Wang, H.; He, D.; Zhou, Y.; Peng, W.; Fan, F.; Huang, H. Transferable and flexible thermoelectric thin films based on elemental tellurium with a large power factor. *Appl. Phys. Lett.* **2018**, *112*, 243904. [[CrossRef](#)]
104. Gao, H.L.; Liu, X.X.; Zhu, T.J.; Yang, S.H.; Zhao, X.B. Effect of Sb Doping on the Thermoelectric Properties of $\text{Mg}_2\text{Si}_{0.7}\text{Sn}_{0.3}$ Solid Solutions. *J. Electron. Mater.* **2011**, *40*, 830–834. [[CrossRef](#)]

105. Du, Z.; Zhu, T.; Chen, Y.; He, J.; Gao, H.; Jiang, G.; Tritt, T.M.; Zhao, X. Roles of interstitial Mg in improving thermoelectric properties of Sb-doped $\text{Mg}_2\text{Si}_{0.4}\text{Sn}_{0.6}$ solid solutions. *J. Mater. Chem.* **2012**, *22*, 6838–6844. [[CrossRef](#)]
106. You, S.; DesArmo, J.; Joo, S. Measuring happiness of US cities by mining user-generated text in Flickr.com: A pilot analysis. *Proc. Am. Soc. Inf. Sci. Technol.* **2013**, *50*, 1–4. [[CrossRef](#)]
107. Liu, W.; Tan, X.; Yin, K.; Liu, H.; Tang, X.; Shi, J.; Zhang, Q.; Uher, C. Convergence of Conduction Bands as a Means of Enhancing Thermoelectric Performance of -Type. Solid Solutions. *Phys. Rev. Lett.* **2012**, *108*, 166601. [[CrossRef](#)]
108. Liu, H.T. Bi₂Se₃-Based Low-Dimensional Nanomaterials. Master's Thesis, Xinjiang University, Xinjiang, China, 2018.
109. Cho, C.; Culebras, M.; Wallace, K.L.; Song, Y.; Holder, K.; Hsu, J.-H.; Yu, C.; Grunlan, J.C. Stable n-type thermoelectric multilayer thin films with high power factor from carbonaceous nanofillers. *Nano Energy* **2016**, *28*, 426–432. [[CrossRef](#)]
110. Hong, M.-H.; Park, C.-S.; Shin, S.; Cho, H.H.; Seo, W.-S.; Lim, Y.S.; Lee, J.-K.; Park, H.-H. Effect of surfactant concentration variation on the thermoelectric properties of mesoporous ZnO. *J. Nanomater.* **2013**, *2013*, 2. [[CrossRef](#)]
111. Hong, M.-H.; Shim, D.I.; Cho, H.H.; Park, H.-H. Effect of mesopore-induced strain/stress on the thermoelectric properties of mesoporous ZnO thin films. *Appl. Surf. Sci.* **2018**, *446*, 160–167. [[CrossRef](#)]
112. Miner, A. The Compatibility of Thin Films and Nanostructures in Thermoelectric Cooling Systems. *J. Heat Transf.* **2006**, *129*, 805–812. [[CrossRef](#)]
113. Fu, J.; Song, S.; Zhang, X.; Cao, F.; Zhou, L.; Li, X.; Zhang, H. Bi₂Te₃ nanoplates and nanoflowers: Synthesized by hydrothermal process and their enhanced thermoelectric properties. *CrystEngComm* **2012**, *14*, 2159–2165. [[CrossRef](#)]
114. Shi, W.; Huo, L.; Wang, H.; Zhang, H.; Yang, J.; Wei, P. Hydrothermal growth and gas sensing property of flower-shaped SnS₂ nanostructures. *Nanotechnology* **2006**, *17*, 2918–2924. [[CrossRef](#)]
115. Kuo, C.-L.; Kuo, T.-J.; Huang, M.H. Hydrothermal Synthesis of ZnO Microspheres and Hexagonal Microrods with Sheetlike and Platelike Nanostructures. *J. Phys. Chem. B* **2005**, *109*, 20115–20121. [[CrossRef](#)] [[PubMed](#)]
116. Li, F.; Ding, Y.; Gao, P.; Xin, X.; Wang, Z.L. Single-Crystal Hexagonal Disks and Rings of ZnO: Low-Temperature, Large-Scale Synthesis and Growth Mechanism. *Angew. Chem. Int. Ed.* **2004**, *43*, 5238–5242. [[CrossRef](#)] [[PubMed](#)]
117. Brinker, C.J.; Lu, Y.; Sellinger, A.; Fan, H. Evaporation-Induced Self-Assembly: Nanostructures Made Easy. *Adv. Mater.* **1999**, *11*, 579–585. [[CrossRef](#)]